Impact of seasonal temperature and pressure changes on methane gas production, dissolution, and transport in unfractured sediments

J. M. Mogollón,[1] A. W. Dale,[2] I. L'Heureux,[3] and P. Regnier[1,4]

[1] A one-dimensional reaction-transport model is used to investigate the dynamics of methane gas in coastal sediments in response to intra-annual variations in temperature and pressure. The model is applied to data from two shallow water sites in Eckernförde Bay (Germany) characterized by low and high rates of upward fluid advection. At both sites, organic matter is buried below the sulfate-reducing zone to the methanogenic zone at sufficiently high rates to allow supersaturation of the pore water with dissolved methane and to form a free methane gas phase. The methane solubility concentration varies by similar magnitudes at both study sites in response to bottom water temperature changes and leads to pronounced peaks in the gas volume fraction in autumn when the methanic zone temperature is at a maximum. Yearly hydrostatic pressure variations have comparatively negligible effects on methane solubility. Field data suggest that no free gas escapes to the water column at any time of the year. Although the existence of gas migration cannot be substantiated by direct observation, a speculative mechanism for slow moving gas is proposed here. The model results reveal that free gas migrating upward into the undersaturated pore water will completely dissolve and subsequently be consumed above the free gas depth (FGD) by anaerobic oxidation of methane (AOM). This microbially mediated process maintains methane undersaturation above the FGD. Although the complexities introduced by seasonal changes in temperature lead to different seasonal trends for the depth-integrated AOM rates and the FGD, both sites adhere to previously developed prognostic indicators for methane fluxes based on the FGD.

1. Introduction

[2] Methanogenesis occurs in continental shelf sediments receiving a large supply of bioavailable particulate organic carbon (POC). Although a relatively small fraction of the POC, on average 5% [*Jørgensen and Kasten*, 2006], is degraded by microbes via methanogenesis following mixing and burial below the sulfate (SO_4^{2-}) reducing zone, the rate of methanogenesis may become sufficiently high that the accumulation of dissolved methane eventually exceeds the local methane solubility concentration ($C_{CH_4}^*$), and methane gas bubbles form in the interstitial pore water. Since the solubility of a gas increases with pressure, free methane gas is commonly detected in organic-rich, shallow water sediments where the hydrostatic pressure is relatively low [*Martens and Klump*, 1980; *Martens et al.*, 1998].

[3] Free methane gas formed at depth may either become trapped in the sediment or migrate toward the sediment-water interface (SWI). Migrated gas, in turn, may either redissolve in the pore water or escape directly into the water column [e.g., *Martens and Klump*, 1980]. Dissolved methane can be used as an energy substrate by microorganisms which oxidize methane by oxygen at the SWI or anaerobically using the downward diffusing sulfate as the terminal electron acceptor rather than oxygen. Anaerobic oxidation of methane (AOM) occurs in the sulfate-methane transition zone (SMTZ) and is a major barrier to methane emissions from marine sediments to the ocean-atmosphere [*Claypool and Kaplan*, 1974; *Reeburgh*, 2007; *Regnier et al.*, 2011]. An adequate description of these alternative, parallel anaerobic methane cycling pathways is instrumental to the quantification and forecasting of methane emissions from marine sediments.

[4] Physical and biogeochemical controls on methane cycling in marine sediments are complex. For example,

[1]Department of Earth Sciences, Utrecht University, Utrecht, Netherlands.
[2]Leibniz-Institut für Meereswissenschaften, IFM-Geomar, Kiel, Germany.
[3]Department of Physics, University of Ottawa, Ottawa, Ontario, Canada.
[4]Département des Sciences de la Terre et de l'Environnement, Université Libre de Bruxelles, Bruxelles, Belgium.

Table 1. Methane-Related Features at Eckernförde Bay Investigated Sites[a]

	SMTZ Depth[b] (cm)	FGD (cm)	$\sum$AOM Rate (mmol m^{-2} yr^{-1})
Low Fluid Advection Sites			
Abegg and Anderson [1997]	0	60[c]	ND
Anderson et al. [1998]	ND	15–85[d]	ND
Treude et al. [2005]	10–22	ND	100–500[d]
Martens et al. [1998]	26	90[e]	426[e]
Mogollón et al. [2009]	23[e]	60[e]	321[e]
Bussmann et al. [1999]	25	ND	511
Wever et al. [2006]	ND	80–50[f]	ND
Wever et al. [1998]	0	80–40[f]	ND
This study	28–29	72–50	310–470
High Fluid Advection Sites			
Abegg and Anderson [1997]	0	6[c]	ND
Albert et al. [1998]	1	25[e]	ND
Bussmann et al. [1999]	5	ND	1425
This study	7.5–10	29–13	900–1500

[a]ND, no data.
[b]When sulfate measurements were not available, defined as depth to 0.1 mM CH_4.
[c]Based on computed-tomography bubble counts.
[d]May not include the full AOM zone.
[e]Simulated steady state results.
[f]Based on acoustic profiling.

microbial reactions implicated in methane cycling have been observed to depend on temperature both in the field [*Jørgensen*, 1977; *Treude et al.*, 2005] and in the laboratory [*Crill and Martens*, 1983]. In shallow waters (<50 m), seasonal bottom water temperature variations can lead to differential heat penetration into the sediment and may affect the kinetics of the local microbial-induced reaction rates, including methanogenesis and AOM [*Dale et al.*, 2008a; *Treude et al.*, 2005]. Furthermore, upward advection of pore water not only influences the transport of methane but can also influence the thickness of the sulfate reduction zone and affect the $C^*_{CH_4}$ through variations in salinity [*Albert et al.*, 1998]. Thirdly, the generation and dissolution of free methane gas can provide important feedbacks on dissolved methane [*Mogollón et al.*, 2009]. The latter processes are highly dependent on the molar transfer rate between the gaseous and aqueous phases. These processes are typically depicted [e.g., *Dale et al.*, 2008a; *Haeckel et al.*, 2004; *Mogollón et al.*, 2009] as being dependent on the departure from the local $C^*_{CH_4}$, which in turn depends on the local temperature, pressure, and salinity [*Duan and Mao*, 2006].

[5] *Dale et al.* [2009] determined that the free gas depth (FGD), that is, the depth at which free methane gas is first detected in the sediment, can be used as a potential diagnostic indicator for depth-integrated AOM rates. Although this approach was founded on the steady state approximation, the predictions of the model were robust for a large number of parameters and FGDs > 1 m below the seafloor. Yet, an apparent temperature-induced seasonality in the FGD has been observed [*Wever and Fiedler*, 1995]. These authors reconstructed the annual variability of the in situ sediment temperature from changes in the FGD and from the lag time for heat diffusion into the sediment with respect to bottom water temperatures. A more recent acoustic survey over a 4 month period by *Wever et al.* [2006] again showed clear temporal variations in the FGD.

[6] Here, we apply a reactive-transport model (RTM) to identify the biogeochemical or physical factors which contribute to short-term changes in the FGD, the episodes of enhanced free gas transport, and their relation to dissolved methane, AOM and intensity of upward pore water advection. The current model is based on an earlier construct by *Mogollón et al.* [2009], who developed a three-phase (gas, aqueous, solid), 1-D numerical RTM which included mass and momentum conservation to describe a collective gas bubble phase in an unconsolidated sediment matrix. The model is based on diffusion-dominated growth of a collective gas phase and was calibrated to the diffusion-limited constant eccentricity and linear elastic fracture mechanic (LEFM) growth approach for a single bubble in the work by *Gardiner et al.* [2003a, 2003b] and *Algar and Boudreau* [2009], respectively. The model also includes externally impressed fluid flow as well as the feedback of the gas phase on the sediment physics. *Mogollón et al.* [2009] used the model to examine the transport and dissolution of free methane gas in sediments at the Naval Research Laboratory (NRL) location in Eckernförde Bay (Germany) where freshwater fluids percolate upward through the sediment at a rate of 1 cm yr^{-1}. Under steady state conditions, the model reproduced the general trends in measured geochemical concentrations and rates, the depth of the sulfate-methane transition zone (SMTZ), as well as the gas volume fractions. It also predicted that gas transport can increase the dissolved methane concentration immediately above the depth horizon where the FGD occurs, thereby enhancing AOM.

[7] In this study, we revisit the NRL site with the goal of understanding the seasonal dynamics of the methane cycle, and use the interannual FGD data of *Wever et al.* [1998] at three nearby sites to constrain free methane gas dissolution rates and the effect on methane turnover rates. We also apply the model to a site where extensive fluid seepage has caused a depression in the sediment, that is, a pockmark site, also located in Eckernförde Bay, where externally imposed fluid advection rates reach 10 cm yr^{-1} [*Albert et al.*, 1998].

2. Site Description

[8] Eckernförde Bay is situated on the northern German coast within Kiel Bight (Baltic Sea). It is characterized by relatively shallow waters (0–29 m) and elevated fine-particle sediment burial velocities (0.1–0.6 cm yr^{-1}) [*Martens et al.*, 1998; *Nittrouer et al.*, 1998]. Previous geochemical and geophysical studies [*Wever and Fiedler*, 1995; *Wever et al.*, 2006] have revealed widespread acoustic turbidity, caused by the presence of free methane gas, and small pockmarks. Seasonal changes in the depth of acoustic turbidity in the sediment, the depth of the SMTZ, and the microbial sulfate reduction and AOM rates have also been reported [*Martens et al.*, 1998, 1999; *Treude et al.*, 2005; *Wever and Fiedler*, 1995; *Wever et al.*, 2006]. The geochemical profiles and the SMTZ depth indicate that the depth of methane gas is highly variable throughout the bay (see Table 1). This variation has been attributed to the intensity of freshwater advection, the sediment topography and POC flux to the seafloor [*Abegg and Anderson*, 1997; *Albert et al.*, 1998]. In this study, we investigate two sites with different fluid flow regimes: the NRL site and a pockmark site. Groundwater seepage rates at these sites have been determined based on chloride profiles to

Table 2. Model Variables

Name	Symbol	Unit
Time	t	years
Depth in sediment	z	cm
Solid volume fraction	ϕ_s	
Aqueous volume fraction	ϕ_a	
Gas volume fraction	ϕ_g	
Porosity	φ	
Solid phase velocity	v_s	cm yr^{-1}
Aqueous phase velocity	v_a	cm yr^{-1}
Gas phase velocity	v_g	cm yr^{-1}
Diffusion coefficient for species i	D_i	cm^2 yr^{-1}
Pressure	P	bars
Temperature	T	K
Chloride concentration	C_{Cl^-}	mM
Dissolved methane concentration	C_{CH_4}	mM
Sulfate concentration	$C_{SO_4^{2-}}$	mM
POC concentration	C_{POC}	%
Radius of methane gas bubbles	r	cm
Bubble density	n	cm^{-3}

be 1 cm yr^{-1} [*Albert et al.*, 1998; *Martens et al.*, 1998] and 10 cm yr^{-1} [*Albert et al.*, 1998] respectively.

3. Methodology

3.1. Model Setup

[9] Seasonal simulations over time (t) for a 1-D sediment profile over depth (z) in Eckernförde Bay were performed over the first 10 meters of sediment using a variation of the model developed by *Mogollón et al.* [2009]. The model explicitly includes the solid phase (ϕ_s), aqueous (ϕ_a) and gas (ϕ_g) volume fractions (Table 2). The model assumes that the solid and aqueous phases are incompressible under the range of temperature and pressure variations investigated here. The porosity (φ) is defined as the sum of the fluid phase volume fraction ($\varphi = \phi_a + \phi_g$). The sediments are subjected to steady state compaction ($\partial\varphi/\partial t = 0$), which yields a decreasing porosity value with increasing depth [*Mogollón et al.*, 2009]. The reader is referred to Appendix A for a brief formulation of the model. Expressions for the solid phase burial velocity, v_s, and the aqueous phase velocity, v_a, are also given in Appendix A.

[10] Although the gas phase in muddy sediments exists as discrete bubbles, the mechanism of gas transport through the sediments in reactive transport models has been implemented assuming that these bubbles can be represented collectively as a continuous gas phase. Such an approach has been used to quantify gas burial [*Davie and Buffett*, 2001], gas advecting with pore water [*Buffett and Archer*, 2004], upward gas diffusion [*Dale et al.*, 2008a], or slow advection [*Mogollón et al.*, 2009]. While experiments in gels, used as a surrogate for muddy sediments, have revealed that bubbles move at the centimeter per second scale through fracturing [*Boudreau et al.*, 2005; *Algar et al.*, 2011], we explore here the possibility for the onset of an upward gas movement which is sufficiently slow to allow for gas redissolution within the SMTZ, thus providing an extra methane source for AOM. The viability of our proposed mechanism is highly dependent on the ability for the gas phase to overcome the pore entry pressure (see below) and depends on factors such as the grain size diameter, the contact angle between the gas, aqueous and solid phases, and the size of the bubble. Although our proposed mode of transport is speculative, its possible occur-

rence may be viable in settings such as Eckernförde Bay, where pore water advection may reduce the effects of capillary pressure and induce interstitial bubble movement. To our knowledge direct observations on interstitial gas transport in sediments are still lacking. In sediments housing free methane gas, however, very steep methane gradients [*Whiticar*, 2002] as well as unusually high AOM rates [*Treude et al.*, 2005] have been interpreted as evidence for gas redissolution in the methane-undersaturated zone. By using a model approach, we quantify the rates at which gas moves through these sediments using geochemical observations, mainly the methane and sulfate gradients, as possible indirect indicators of gas migration and redissolution. While this approach certainly leads to a simplification of the complexities involved in interstitial gas transport, our model attempts to study the possible feedbacks of the gas phase on dissolved methane and AOM. We rediscuss some of the limitations of our proposed mechanism for gas migration at the end of this manuscript. We quantify the interstitial free gas velocity, v_g, (henceforth termed free gas velocity) using momentum balance for a gas phase in a three-phase system where each phase moves individually [*Mogollón et al.*, 2009]:

$$v_g = \frac{\varepsilon d^2}{\eta_g\left(\phi_s^2 + \phi_a^2\right)}\left(-\frac{\partial P}{\partial z} + \frac{2\gamma}{r^2}\frac{\partial r}{\partial z} + \frac{MP}{\Re T}g\right)\phi_g^2$$
$$+ \frac{\phi_s^2 v_s}{\left(\phi_s^2 + \phi_a^2\right)} + \frac{\phi_a^2 v_a}{\left(\phi_s^2 + \phi_a^2\right)} \quad (1)$$

where P is the pressure, d is the average grain size diameter, η_g is the viscosity of the gas phase, ε the Carman-Kozeny constant, which describes the shape and interconnectivity of the pores, γ is the surface tension of the bubble, r is the average bubble radius, g is the acceleration due to gravity, M is the methane molecular weight, $\Re$ is the universal gas constant and T is the temperature. In equation (1), r is an explicit variable for the model (Table 2). This equation allows for the physical description of a dynamic three-phase system in a 1-D framework, representing the collective movement of the FGD. It does not describe gas movement due to canalization or fracture formation, which demands an entirely different set of physical equations [*Haeckel et al.*, 2007; *Stöhr and Khalili*, 2006; *Algar et al.*, 2011] and are not typically observed in the gassy areas of the Baltic Sea [*Laier and Jensen*, 2007]. To our knowledge, no measurements of gas velocities for single bubbles or the advective gas phase have been performed in muddy marine sediments that can either support or disprove our mechanistic representation (equation (1)). At this stage, our proposed theory remains therefore speculative.

[11] Heat transport through sediments can be described by the specific heat capacities and thermal conductivities of the solid, aqueous and gaseous phases [*Woodside and Messmer*, 1961]. With the assumption that heat generated/lost during methane-phase transitions is negligible, the conservation equation for temperature is the following:

$$\frac{\partial T}{\partial t} = -\frac{\partial}{\partial z}\left(\frac{c_s\rho_s\phi_s v_s + c_a\rho_a\phi_a v_a + c_g\frac{MP}{\Re T}\phi_g v_g}{c_s\rho_s\phi_s + c_a\rho_a\phi_a + c_g\frac{MP}{\Re T}\phi_g}T\right) + \frac{\partial}{\partial z}\left(D_T\frac{\partial T}{\partial z}\right)$$
$$(2)$$

where c, ρ, represent the specific heat capacity, and density, for the solid (s), aqueous (a) and gas (g) phases. The first

Table 3. Fixed Parameters

Name	Symbol	Value	Unit	Source
Dispersivity	α	1.0	cm	this study
Methane mass transfer coefficient	β	100	cm yr^{-1}	this study
Specific heat capacity (aqueous phase)	c_a	4.184	J g^{-1} K^{-1}	Woodside and Messmer [1961]
Specific heat capacity (gas phase)	c_g	2.0	J g^{-1} K^{-1}	Woodside and Messmer [1961]
Specific heat capacity (solid phase)	c_s	0.3	J g^{-1} K^{-1}	Woodside and Messmer [1961]
Bubble diffusive boundary layer constant	c_λ	0.38	–	Algar and Boudreau [2009][a]
Average grain size diameter	d	2×10^{-4}	cm	Silva and Brandes [1998]
Methane bubble surface tension	γ	32	dyne cm^{-1}	this study
Methane activation energy	E_{CH_4}	18.36	kJ mol^{-1}	Boudreau [1997]
Carman-Kozeny constant	ε	0.003	–	this study
Methane gas viscosity	η_g	0.0001027	Poise	this study
Thermal conductivity (aqueous phase)	k_a	0.6	W m^{-1} K^{-1}	Woodside and Messmer [1961]
Thermal conductivity (gas phase)	k_g	0.3	W m^{-1} K^{-1}	Woodside and Messmer [1961]
Thermal conductivity (solid phase)	k_s	2.5	W m^{-1} K^{-1}	Woodside and Messmer [1961]
Zero rate constant for AOM	k_{AOM}	50	mM^{-1} yr^{-1}	this study
First concentration for sulfate diffusion	$m_{0,SO_4^{2-}}$	4.88	10^{-6} cm^2 s^{-1}	Boudreau [1997]
First concentration for chloride diffusion	m_{0,Cl^-}	9.6	10^{-6} cm^2 s^{-1}	Boudreau [1997]
First concentration for methane diffusion	m_{0,CH_4}	0.03047	cm^2 s^{-1}	Boudreau [1997]
Second concentration for sulfate diffusion	$m_{1,SO_4^{2-}}$	0.232×10^{-6}	cm^2 s^{-10} C^{-1}	Boudreau [1997]
2nd const. for chloride diffusion	m_{1,Cl^-}	0.438×10^{-6}	cm^2 s^{-10} C^{-1}	Boudreau [1997]
Average atmospheric pressure	P_{atm}	1013	hPa	this study
Reference temperature	T_{ref}	277.13	K	Dale et al. [2008a]
Density (aqueous phase)	ρ_a	1.01	g cm^{-3}	this study
Density (solid phase)	ρ_s	2.6	g cm^{-3}	this study
Half saturation concentration for sulfate	$K_{SO_4^{2-}}$	0.1	mM	Dale et al. [2008a]
Half saturation concentration for methane	K_{CH_4}	1.0	mM	Dale et al. [2008a]
Ideal gas constant	$\Re$	8.3144	J K^{-1} mol^{-1}	
Rate constant temperature correction	Q_{10}	3.8	–	Dale et al. [2008a]

[a]Parameter was indirectly constrained with data from this study.

term on the right hand side describes heat advection and the second term heat conduction. The thermal diffusivity coefficient, D_T, is defined as the random distribution geometric mean of the diffusivity for all three phases [Woodside and Messmer, 1961]:

$$D_T = \frac{k_s^{\phi_s} k_a^{\phi_a} k_g^{\phi_g}}{c_s \phi_s \rho_s + c_a \phi_a \rho_a + c_g \phi_g \frac{MP}{\Re T}} \quad (3)$$

where k_x is the thermal conductivity for phase x. In writing equations (2) and (3) the quantity $[c_s \phi_s \rho_s + c_a \phi_a \rho_a + c_g \phi \frac{MP}{\Re T}]$ was considered constant. Also, in treating equations (2) and (3) the nonlinear behavior due to the weak temperature dependence of the thermal diffusivity has been neglected.

[12] Mass conservation equations are included for 4 chemical components: dissolved methane, sulfate, chloride (Cl^-), and POC. The change in concentration of solid species, C_j (mole (g dry sed)$^{-1}$), with time is given by:

$$\frac{\partial (1-\varphi) C_j}{\partial t} = -\frac{\partial [v_s (1-\varphi) C_j]}{\partial z} + (1-\varphi) \sum R_j \quad (4)$$

where $\sum R_j$ represents the net biogeochemical reaction rate. In this study, POC is the only solid species considered.

[13] Simulated concentrations of aqueous species, C_i, (methane, sulfate, chloride, all in mM) depend on the fluid advection, component specific diffusion/dispersion, and reaction:

$$\frac{\partial \phi_a C_i}{\partial t} = -\frac{\partial (v_a \phi_a C_i)}{\partial z} + \frac{\partial}{\partial z}\left(D_i^* \phi_a \frac{\partial C_i}{\partial z}\right) + \phi_a \sum R_i \quad (5)$$

where v_a is the aqueous phase advection, $\sum R_i$ is the net reaction rate affecting species i ($= 0$ for chloride), and D_i^* is

the effective hydrodynamic dispersion coefficient for the solute. D_i^* depends on the tortuosity and the dispersivity (α) of the sediment [Boudreau, 1997],

$$D_i^* = \alpha v_a + \frac{D_i}{1 - 2\ln(\varphi)} \quad (6)$$

where D_i is the temperature-dependent molecular diffusion coefficient of species i at in situ salinity, and α is the dispersivity constant. D_i is calculated by a linear regression with temperature (equation (7)) for the sulfate and Cl^- anions [Boudreau, 1997]:

$$D_i = m_{0,i} + m_{1,i}(T - 273.15) \quad (7)$$

where $i = SO_4^{2-}, Cl^-$. $m_{0,i}, m_{1,i}$ are fitting parameters, and T is the temperature in K. The diffusion coefficient for methane is modeled by an Arrhenius-type dependence on temperature [Boudreau, 1997]:

$$D_i = m_{0,i} e^{\left(\frac{-E_i}{\Re T}\right)} \quad (8)$$

where $i = CH_4$. $m_{0,i}$ is a fitting parameter, and E_i is the activation energy for methane diffusion (Table 3).

[14] Salinity was calculated from chlorinity (in mM) [Albert et al., 1998] using $S = 0.03 + 35.45 \times C_{Cl^-} 1.01 \times 10^{-3} \times 1.8065$ [Ehrhardt et al., 1983]. In Eckernförde Bay sediments, the extensive preservation of laminae suggests that bioturbation and bioirrigation are absent or negligible [Nittrouer et al., 1998] and, thus, these processes were not included in the model.

[15] Wever and Fiedler [1995] and Wever et al. [2006] reported that methane is the dominant gas in Eckernförde Bay sediments, with traces of hydrogen sulfide and carbon

dioxide present. Accordingly, the free gas phase was assumed to be composed entirely of methane and move according to a gas velocity, v_g, derived from equation (1). The mass balance equation for the gas phase (assuming a constant bubble density, n) scales to the growth of the bubble radius due to gas formation/dissolution and the advective bubble transport (Appendix A):

$$\frac{\partial r^3 P/T}{\partial t} = -v_g \frac{\partial r^3 P/T}{\partial z} + 3r^2 \frac{P}{T} \psi \qquad (9)$$

The last term on the right hand side of equation (9) represents the radius growth due to the molar transfer of methane from the aqueous phase. The methane mass transfer rate, ψ, is defined as

$$\psi \equiv \begin{cases} \dfrac{\psi_D \psi_{IC}}{\psi_D + \psi_{IC}} & (C_{CH_4} \geq C_{CH_4}^*) \\ \psi_{IC} & (C_{CH_4} < C_{CH_4}^*) \end{cases} \qquad (10)$$

$$\psi_{IC} = \beta \left(\frac{C_{CH_4} - C_{CH_4}^*}{C_{CH_4}^*} \right) \qquad (11)$$

$$\psi_D = \frac{D_i \Re T}{P \lambda} \left(C_{CH_4} - C_{CH_4}^* \right) \qquad (12)$$

where β is the methane mass transfer coefficient, ψ_D is the diffusion-controlled gas growth rate, ψ_{IC} is the interface-controlled gas growth/dissolution rate and $C_{CH_4}^*$ is the methane solubility concentration. λ is the thickness of the diffusive boundary layer, here defined as $\lambda = c_\lambda r$, where c_λ is a fitting constant which was adjusted to the bubble growth times of the diffusion limited constant eccentricity model of *Gardiner et al.* [2003b] through the following equation (see Appendix B):

$$c_\lambda = \frac{\arccos(E_{cc}) E_{cc}^{1/3}}{\left(1 - E_{cc}^2\right)^{0.5}} \qquad (13)$$

where E_{cc} is the aspect ratio of the bubble, which denotes the width-to-length ratio of the bubble. The aspect ratio for bubbles has only been qualitatively analyzed, with shapes ranging from near spherical to near coin shaped [*Anderson et al.*, 1998]. Thus we require an additional calibration parameter to determine a suitable aspect ratio for bubbles. In *Gardiner et al.* [2003a] linear elastic fracture mechanics (LEFM) and diffusion limited constant eccentricity (DLCE) growth times were compared, with an aspect ratio of 0.036 (or a c_λ of 0.526) closely approximating the LEFM growth times of a 0.5 mL bubble. In *Algar and Boudreau* [2009], however, the LEFM growth times were corrected to account for a fully transient model and the introduction of Poisson's ratio to the equations, lowering the growth time of a 0.5 mL bubble by ~28%, which in our algorithm represents a value for c_λ of ~0.38. This latter value was used in the present study.

3.2. Reaction Network

[16] Assuming that extracellular hydrolysis of POC is the rate-determining step in the mineralization of marine organic matter, the rate can be described with a first-order formulation with respect to labile POC:

$$R_{POC} = Q_{10}^{\frac{T - T_{ref}}{10}} k_{POC} C_{POC} \qquad (14)$$

where k_{POC} is the 1st order degradation rate constant, and Q_{10} represents the reaction sensitivity toward temperature (T in K) variations with respect to a reference temperature (T_{ref} in K). Note that for POC in equation (4), $\sum R_{POC} = - R_{POC}$.

[17] POC is defined chemically as carbohydrate (CH_2O) and assumed to be degraded through sulfate reduction: $CH_2O_{(s)} + 0.5SO_{4(aq)}^{2-} + H_{(aq)}^+ \rightarrow H_2O + CO_{2(aq)} + 0.5H_2S_{(aq)}$ and methanogenesis: $CH_2O_{(s)} \rightarrow 0.5CH_{4(aq)} + 0.5CO_{2(aq)}$. Sulfate reduction inhibits methanogenesis until sulfate concentration falls below a limiting concentration, $K_{SO_4^{2-}}$. The rates of sulfate reduction, R_{SR}, and methanogenesis, R_{MET}, are thus given by:

$$R_{SR} = f_{SO_4^{2-}} \frac{(R_{POC})}{2} \rho_s \frac{(1 - \varphi)}{\phi_a} \qquad (15)$$

$$R_{MET} = \left(1 - f_{SO_4^{2-}} \right) \frac{(R_{POC})}{2} \rho_s \frac{(1 - \varphi)}{\phi_a} \qquad (16)$$

with,

$$f_{SO_4^{2-}} \equiv \begin{cases} \dfrac{C_{SO_4^{2-}}}{K_{SO_4^{2-}}} & \text{if } \dfrac{C_{SO_4^{2-}}}{K_{SO_4^{2-}}} \leq 1; \\ 1 & \text{if } \dfrac{C_{SO_4^{2-}}}{K_{SO_4^{2-}}} > 1. \end{cases} \qquad (17)$$

R_{GAS} (equation (18)) defines the transfer rate of methane from the aqueous phase into the gas phase (when ψ is positive) and viceversa (when ψ is negative):

$$R_{GAS} = \frac{4\pi r^2 n P}{\Re T} \psi \qquad (18)$$

[18] Sulfate and methane are also consumed by AOM: $CH_{4(aq)} + SO_{4(aq)}^{2-} + 2H_{(aq)}^+ \rightarrow 2H_2O + H_2S_{(aq)} + CO_{2(aq)}$. AOM was implemented using Michaelis-Menten kinetics, for methane and sulfate and also depends on temperature:

$$R_{AOM} = Q_{10}^{\frac{T - T_{ref}}{10}} k_{AOM} \frac{C_{CH_4}}{C_{CH_4} + K_{C_{CH_4}}} \frac{C_{SO_4^{2-}}}{C_{SO_4^{2-}} + K_{C_{SO_4^{2-}}}} \qquad (19)$$

With the biogeochemical reactions defined, the net reaction rates ($\sum R$) for sulfate and dissolved methane are equal to:

$$\sum R_{SO_4^{2-}} = -R_{SR} - R_{AOM} \qquad (20)$$

$$\sum R_{CH_4} = R_{MET} - R_{AOM} - R_{GAS} \qquad (21)$$

3.3. Methane Solubility

[19] The methane solubility concentration, $C_{CH_4}^*$, is a function of pressure P, temperature T, and salinity S. Although the $C_{CH_4}^*$ has been previously estimated using a 3rd order polynomial in Aarhus Bay and Eckernförde Bay sediments [*Dale*

Table 4. Site-Dependent Parameters and Boundary Conditions[a]

Name	Symbol	NRL	Pockmark	Unit
Sedimentation rate[b]	$v_s\vert_L$	0.6	0.6	cm yr^{-1}
T amplitude (SWI)	A_0	4	4	K
T time lag (SWI)	θ_0	0.548	0.548	year
Sea level amplitude	$\overline{A_{sea}}$	4.8	4.8	cm
Average sea level	$\overline{h_{sea}}$	25	21	m
Sea level time lag	θ_{sea}	0.55	0.55	year
POC decay time constant	k_{POC}	0.003	0.003	yr^{-1}
Imposed aqueous advection	$q_a\vert_L$	1.0	10.0	cm yr^{-1}
Average temperature (SWI)	$\overline{T_0}$	279.5	279.5	K
Average temperature (L)	$\overline{T_L}$	279.5	279.5	K
Methane concentration (SWI)	$C_{CH_4}\vert_0$	0	0	mM
Sulfate concentration (SWI)	$C_{SO_4^{2-}}\vert_0$	18	18	mM
Chloride concentration (SWI)	$C_{Cl^-}\vert_0$	327	327	mM
Methane concentration (L)	$C_{CH_4}\vert_0$	0	0	mM
Sulfate gradient (L)	$\partial C_{SO_4^{2-}}/\partial z\vert_L$	0	0	mM cm^{-1}
Chloride gradient (L)	$\partial C_{Cl^-}/\partial z\vert_L$	0	$C_{Cl^-}\vert_L = 0$ mM	mM cm^{-1}
Flux of reactive POC	F_{POC}	1.2	3.0	mol C m^{-2} yr^{-1}
Bubble density	n	0.2	0.2	cm^{-3}
Bubble radius (L)	r_L	3×10^{-7}	3×10^{-7}	cm
Porosity (SWI)	$\varphi\vert_0$	0.85	0.85	
Porosity (great depth)	$\varphi\vert_\infty$	0.72	0.72	

[a]L, lower boundary.
[b]Below the compacted layer.

et al., 2008a; *Mogollón et al.*, 2009], the broader ranges of pressure, temperature, and salinity investigated here (4–8 bar, 274–286 K, 0–25) required a different algorithm. $C^*_{CH_4}$ has a power law dependence on temperature, whereas it varies linearly with both salinity and pressure [*Duan and Mao*, 2006]. Using these observations, the following formulation, constrained with data from *Duan and Mao* [2006], was utilized:

$$
\begin{aligned}
C^*_{CH_4} = {} & \left(1 - \frac{S-5}{25}\right)\left(\left(1 - \frac{P-3}{5}\right)\left(1.2344 \times 10^{18} T^{-6.88598}\right)\right. \\
& + \left(\frac{P-3}{5}\right)\left(8.30058 \times 10^{17} T^{-6.95275}\right)\bigg) \\
& + \left(\frac{S-5}{25}\right)\left(\left(1 - \frac{P-3}{5}\right)\left(1.09217 \times 10^{17} T^{-6.61713}\right)\right. \\
& \left. + \left(\frac{P-3}{5}\right)\left(1.59074 \times 10^{17} T^{-6.56333}\right)\right)
\end{aligned}
\tag{22}
$$

where P is in bars, T is in kelvins, and S is unitless.

3.4. Boundary Conditions and Temporal Forcing

[20] Measured concentrations at the SWI ($z = 0$) were imposed for sulfate, dissolved methane and chloride and were assumed to be invariant with time (Table 4). For POC, a constant flux boundary condition at the SWI was applied. A zero gradient condition was applied at the lower boundary for dissolved methane, sulfate and chloride, with the exception of chloride and dissolved methane at the pockmark site where a fixed concentration, invariant with time, was applied [*Albert et al.*, 1998]. Seasonal variations in labile organic matter deposition fluxes were ignored because they have limited effects on the methane dynamics [*Dale et al.*, 2008a].

[21] The temperature at the SWI (T_0) was assumed to be time-dependent through a sinusoidal seasonal variation:

$$
T_0 = \overline{T_0} + A_0 \sin\left[2\pi \frac{(t + \theta_0)}{\tau}\right]
\tag{23}
$$

where $\overline{T_0}$ is the yearly averaged temperature, A_0 the amplitude of the temperature variation, and θ_0 is the sinusoidal time lag with respect to the measured temperature data, and τ is the period of one year.

[22] The imposed seasonal temperature curve at the SWI in Eckernförde Bay sediments was estimated based on measured temperature data collected at the SWI [*Schlüter et al.*, 2000; *Treude et al.*, 2005] (Figure 1). The bottom
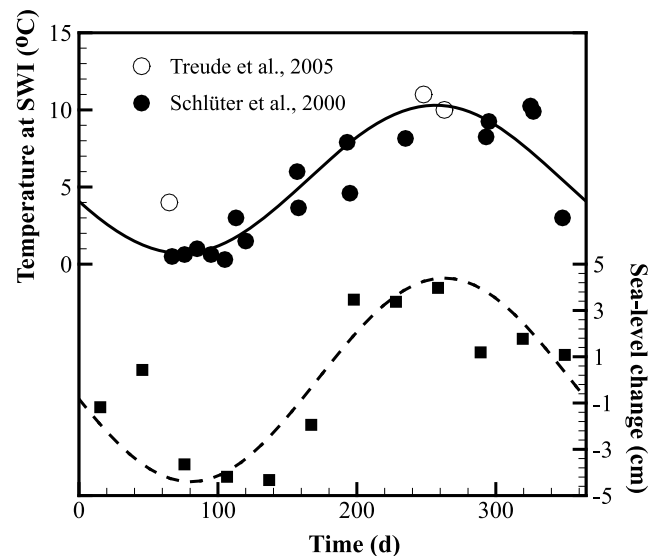
Figure 1. Yearly bottom water temperature and sea level variations for Eckernförde Bay. Circles indicate measured bottom water temperature data at Eckernförde Bay, and squares represent measured gauge data (see text). The solid curve represents the best fit bottom water temperatures as predicted by equation (23). Dashed lines represent the best fit sea level curve using equation (24). The curves were imposed in the model as the temperature and pressure variation at the SWI.

Amplitude of temperature variations (°C)
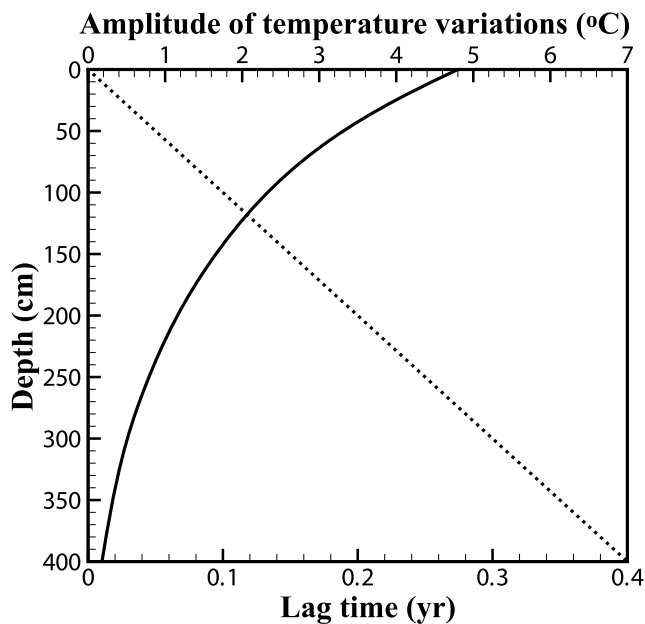
Figure 2. Amplitude of temperature variations in Eckernförde Bay sediments as a function of sediment depth (solid line). The dotted line represents the time lag for the propagation of the maximum temperature with depth, that is, the difference between the timing of the maximum yearly temperature at the SWI and the corresponding timing at any given depth. This lag time is the same for both sites. Note that the differences in pore water advection at the NRL and the pockmark site have a negligible effect on the dynamics of heat propagation.

boundary for temperature $\overline{T_L}$ was located at 10 m depth in the sediment where a constant value $\overline{T_0} = \overline{T_L}$ was specified [*Dale et al.*, 2008a].

[23] The total pressure at the SWI varies according to changes in the atmospheric pressure, as well as changes in the sea level due to tides and winds [*Treude et al.*, 2005; *Wever et al.*, 2006]. The daily tidal range in Eckernförde Bay, however, is small (up to 20 cm with a mean of 5 cm) [*Treude et al.*, 2005] leading to a less than 1% variation in the hydrostatic pressure which, in conjunction with the relatively high frequency for daily tides make the effects on bubble growth negligible [*Algar and Boudreau*, 2009]. Monthly deviations from the yearly mean sea level collected over the last 200 years by the Permanent Service for Mean Sea Level (http://www.pol.ac.uk/psmsl/) were averaged to produce the average yearly tides at Kiel Bight. This data was then fitted with a curve governed by the following expression:

$$h_{sea} = \overline{h_{sea}} + A_{sea} \sin\left[2\pi \frac{(t + \theta_{sea})}{\tau}\right] \qquad (24)$$

where $\overline{h_{sea}}$ is the average water depth, A_{sea} the amplitude of the yearly tidal signal, and θ_{sea} is the time lag with respect to the timing of the average water depth.

[24] All simulations were performed until no interannual variability in the microbial reaction rates and the geochemical species profiles could be observed. The FGD in the simulations was calculated by detecting the depth at which $\phi_g >$ 0.00001, whereas the SMTZ was calculated by finding the depth of equimolar sulfate and methane concentrations.

[25] Section 4 presents how, based on the described model, temperature, pressure, and salinity affect the methane solubility concentration (section 4.1). The model is then validated by comparing simulated results with measured data (section 4.2) and by comparing the simulated intra-annual trends in the FGD to measured data (section 4.3). Based on the seasonal variations in the methane solubility concentration and gas molar volume, we interpret the effects of gas phase formation and dissolution on the anaerobic methane cycle (section 4.4).

4. Results and Discussion

4.1. Temperature and Pressure Effects on Methane Solubility

[26] Bottom water temperature variations at Eckernförde Bay stations (Figure 1) produce a yearly temperature cycle in the sediments which attenuates as it propagates downward (Figure 2). The seasonal temperature cycle can be recorded close to 10 m depth, at which point bottom water temperature variations no longer have an effect [*Dale et al.*, 2008a]. The temperature time lag (the difference between the time of the maximum temperature at the SWI and the corresponding time at a given depth) changes by about 0.1 yr m^{-1}. Heat transport is heavily dominated by conduction, and consequently, the effect of pore water advection at the NRL site ($\simeq 1$ cm yr^{-1}) and the pockmark site ($\simeq 10$ cm yr^{-1}) on the resulting temperature profiles is negligible. Furthermore, changes in the pore water advection do not produce any major changes in the maximum depth at which bottom water temperature variations can be recorded or in the time lags for heat propagation.

[27] Figure 3 shows the values of $C_{CH_4}^*$ computed for the range of P, T, and S conditions recorded at the studied sites. These methane solubility concentrations agree with solubility concentrations from previous studies [*Abegg and Anderson*, 1997; *Dale et al.*, 2008a]. Solubility concentrations are reported from the SWI down to the depth where T variations are less than 1% of those recorded in the bottom waters (800 cm). Using the pockmark site as an example, Figure 3 should be read as follows: At point a, the solubility at the SWI reaches its maximum value of 8.25 mM matching the annual temperature minimum of the bottom water layers. Conversely, point b corresponds to lowest solubility concentrations (6.7 mM) at the highest bottom water temperature. Point c, where the solubility concentration is of 7.4 mM, corresponds to the yearly average bottom water temperature. The attenuating temperature with depth produces the cone-like solubility envelopes, with greater intra-annual solubility variations at the SWI. Point d represents the conditions at 800 cm where the higher pressure (4.5 bar) leads to a solubility increase of ~2 mM compared to the average conditions at the SWI (3.5 bar).

[28] Unlike temperature, which is governed by heat transport and hence subjected to time lags, pressure variations have an immediate and uniform effect on the $C_{CH_4}^*$ throughout the sediment and can shift the entire solubility curve instantaneously. The effect of pressure variations in the sediment associated to daily tides and their long-term modulation are nevertheless minimal since a 20 cm change in the tidal range
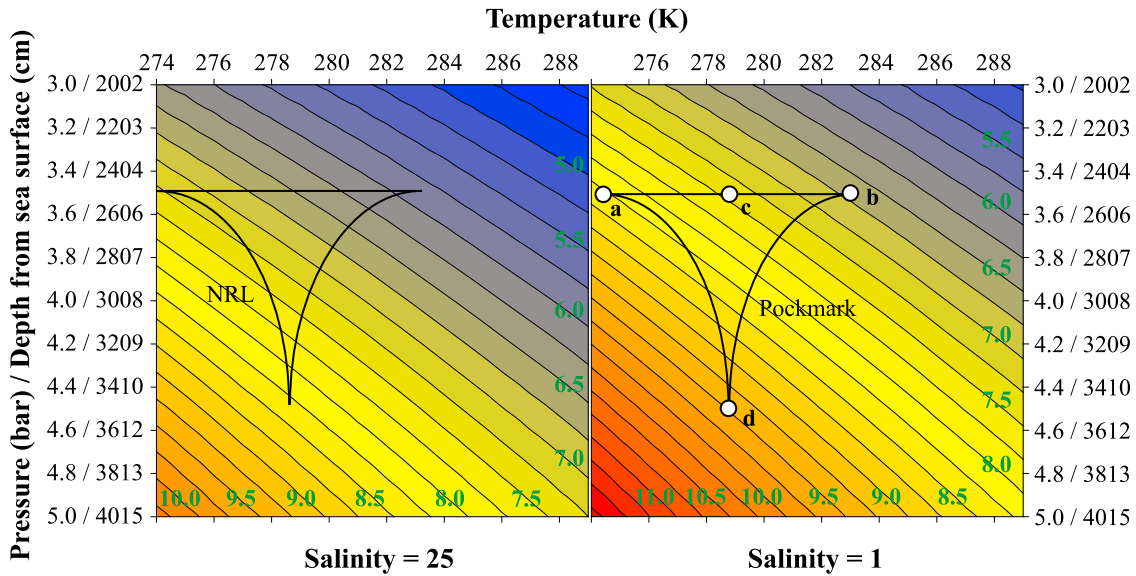
Figure 3. Isolines (thin black lines) of methane solubility ($C^*_{CH_4}$, mM) with respect to T and P using equation (22) with a salinity of 25 and 1 characteristics of the environments investigated in this study. The thick black lines represent the range of solubilities corresponding to the P and T conditions at both sites: (left) NRL and (right) the pockmark. The horizontal positioning of the top of the P-T envelopes gives the approximate position of the SWI. Points a–d are described in the text.

[*Treude et al.*, 2005] represents a shift of ~0.035 mM in $C^*_{CH_4}$ according to equation (22). The pressure variations from Figure 1 imposed in the model are thus too small to be accurately depicted in Figure 3.

[29] It should also be noted that the variation in pore fluid salinity due to variable groundwater seepage can also potentially affect methane solubility [*Albert et al.*, 1998; *Schlüter et al.*, 2004]. However, these seepages, and likewise the salinity profiles, were assumed to be time invariant. Due to groundwater advection, the pockmark site ($q_a|_L =$

$[\varphi(v_a - v_s)]|_L = 10.0$ cm yr^{-1} and $S \simeq 1$) is characterized by $C^*_{CH_4}$ that are roughly 0.6 mM higher than at the NRL site ($q_a|_L = [\varphi(v_a - v_s)]|_L = 1.0$ cm yr^{-1} and $S \simeq 24$) (Figure 3, right) because solubility and salinity are inversely correlated.

4.2. Methane and Sulfate Profiles

[30] The simulated sites exhibit the typical methane and sulfate profiles characteristic of continental shelf sediments where sulfate reduction, methanogenesis, and AOM are prominent (Figure 4). At all sites, sulfate concentrations
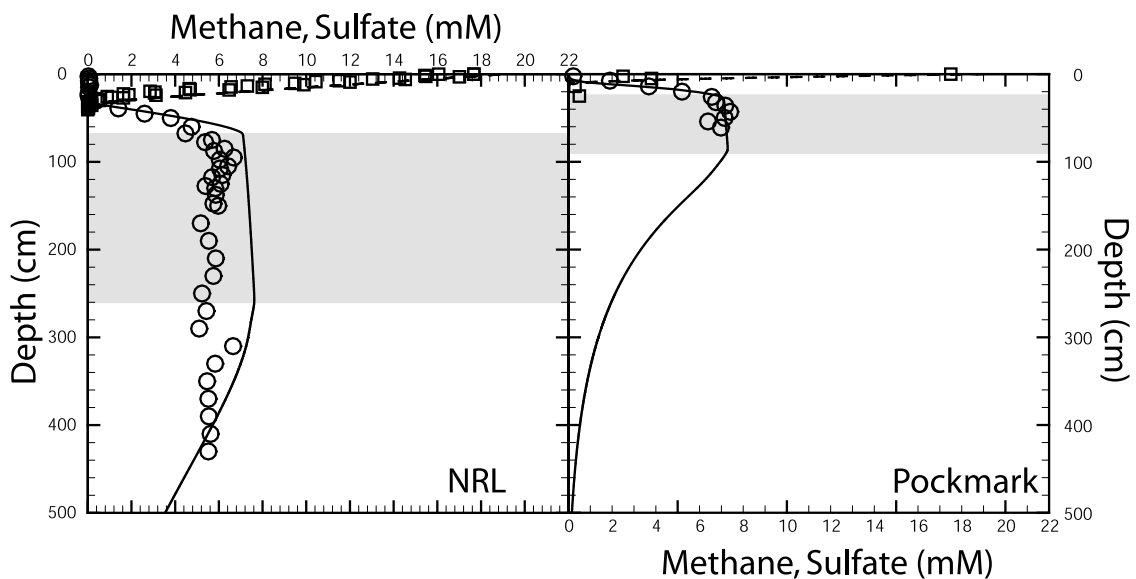
Figure 4. Top 5 m of simulated and measured sulfate (dashed line, open squares) and methane (solid line, circles) profiles at both sites. Gray zones indicate the regions where supersaturation (and thus gas formation) occurs.
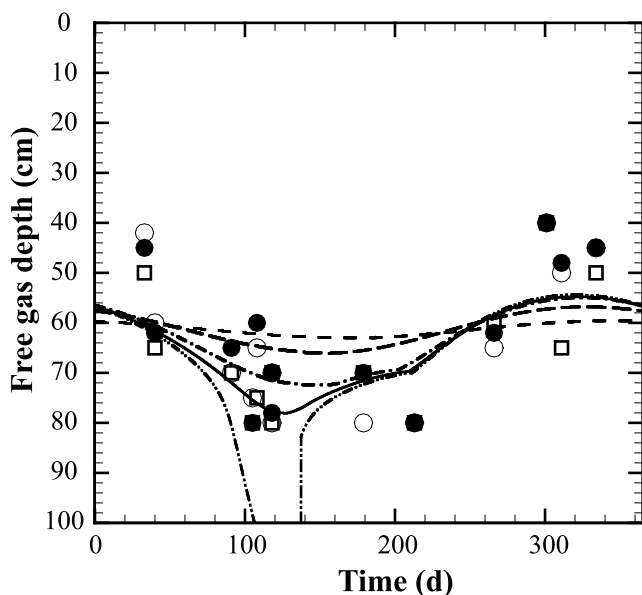
Figure 5. Sensitivity analysis of the seasonal changes in FGD at the NRL site using values for ε of 0.00004 (short dashed line), 0.00041 (long dashed line, predicted value according to data from *Silva and Brandes* [1998]), 0.002 (dash-dotted line), 0.003 (solid line, used as best fit), and 0.004 (dash-dot-dotted line). The results are compared to measured FGDs from acoustic surveys at 3 sites located the following distances away from the NRL site as reported by *Wever et al.* [1998]: 1.8 km (black circles), 1 km (open circles), and 0.8 km (squares).

rapidly decrease from the SWI down to the SMTZ. Likewise, methane gradually increases from sub millimolar values in the SMTZ up to saturation levels (~6 mM) within the first meter of the sediments. Note that measured methane values for the NRL site are lower than their modeled counterparts. This is most likely due to methane degassing during core retrieval and/or during sampling.

[31] Seasonal effects on methanogenesis, AOM, and gas phase formation/dissolution have little impact on the migration of the SMTZ as previously noted by *Dale et al.* [2008a]. At both sites, it is assumed that the methane concentration is close to zero at the lower boundary due to the influence of methane depleted freshwater. The effects of upward advecting freshwater from below on the dilution of dissolved methane concentrations leads to a thinning of the free gas production zone at the pockmark site, as previously observed by *Albert et al.* [1998]. This dilution effect also requires a large POC flux at the pockmark site (3.0 mol m^{-2} yr^{-1}) in order to exceed the methane solubility concentration and form gas, as also observed by *Albert et al.* [1998]. High variability in POC fluxes and burial rates [*Jensen et al.*, 2002], as well as in groundwater advection rates [*Schlüter et al.*, 2004], has been observed within Eckernförde Bay which leads to large horizontal gradients for various geochemical profiles (e.g., chloride, methane, sulfate). Differences in POC fluxes and sediment burial rates are usually the result of the bathymetric evolution of the basin, with topographic depressions accumulating greater amounts of sediment, and, consequently, organic matter [*Albert et al.*, 1998].

4.3. Gas Ascent and Rate of Dissolution

[32] In section 4.1, the range in $C^*_{CH_4}$ was determined based on the temperature dynamics using the heat conduction equation (equation (2)). In addition, gas ascent is derived from momentum conservation for the gas phase which depends on parameters that are inherent properties of the medium and the velocity of the aqueous phase, yielding velocities in the 0–100 cm yr^{-1} range. Although gas ascent in these sediments has not been directly measured, experiments performed in artificial gels seem to suggest that once the sediment has fractured, single bubbles rise with velocities on the order of several centimeters per second [*Algar et al.*, 2011]. In Eckernförde Bay, however, seismic surveys [e.g., *Laier and Jensen*, 2007; *Wever and Fiedler*, 1995; *Wever et al.*, 1998] suggest that gas is either trapped in the sediment or moves at sufficiently slow velocities within the sediment to be captured by acoustic imaging (gas bubbles create acoustic scattering or blanking as opposed to the sedimentary layers). Bubble rise through fractures is not considered in the present study since gas escape at these sites has not been observed [*Martens et al.*, 1998] and velocities induced by gas fracturing the sediment are in the 0.1–10 cm s^{-1} range [*Algar et al.*, 2011]. These velocities would most likely lead to the gas bypassing the AOM zone and thus produce negligible contributions toward seasonality in the methane gradients and in the AOM rates which is the focus of the present study.

[33] Simulated seasonality in the gas phase can be corroborated by comparing modeled and observed FGDs at three locations near the NRL site [*Wever et al.*, 1998] (Figure 5). These observations were based on a 3.5 kHz echo sounder which is able to detect bubbles diameters on the order of millimeters. Measured FGD may vary with usage of different frequencies; nevertheless, minor frequency changes would create minor deviations which would fall within the scatter observed across the FGDs at a given time at the three sites. Although the simulated amplitudes of 24 cm fall short of the observed average variation for all three sites from *Wever et al.* [1998] (~35 cm), the model reproduces the shallower FGDs in the late autumn (October–November) and deeper FGD during the late spring (May–June) (Figure 5). The amplitude of these oscillations is heavily dependent on the sediment parameters described in equation (1) such as the size and sphericity of the grains, as represented by Carman-Kozeny parameter, ε, and the diameter of the sediment grains, d in equation (1), and the hydraulic conductivity, K. The latter two values were measured and averaged for Eckernförde Bay sediments by *Silva and Brandes* [1998] (average $d = 2 \times 10^{-4}$ cm, average $K = 5 \times 10^{-6}$ cm s^{-1}) and can thus be used to make an estimate of ε through the Carman-Kozeny equation used in the model:

$$\varepsilon = \frac{K\phi_s^2\eta_a}{\phi_a^3\rho_a g d^2}$$
$$= \frac{5 \times 10^{-6}\,\text{cm s}^{-1} \times 0.27^2 \times 0.017\,\text{g cm}^{-1}\,\text{s}^{-1}}{0.73^3 \times 1.013\,\text{g cm}^{-3} \times 980\,\text{cm s}^{-2}(2 \times 10^{-4}\,\text{cm})^2}$$
$$= 4.01 \times 10^{-4} \tag{25}$$

where η_a is the dynamic viscosity of the aqueous phase. The resulting value for ε is about seven times lower than the best fit value obtained in the model (Figure 5), which is indicative
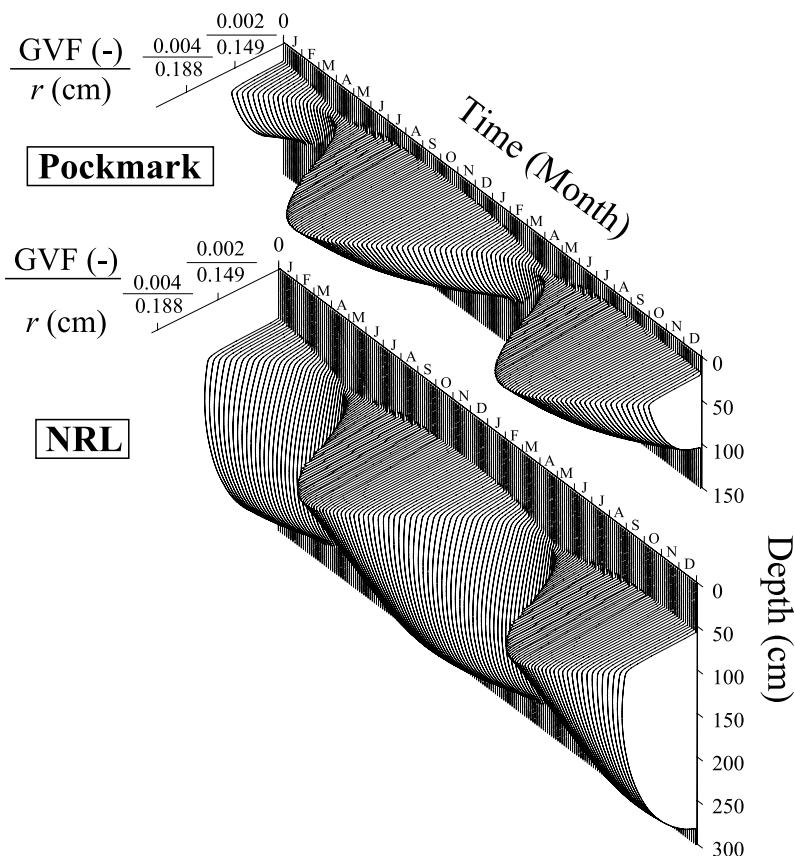
Figure 6. Two year (seasonally dynamic) steady state simulation for gas volume fraction (GVF) and radius (r) with respect to depth at (top) the pockmark site and (bottom) the NRL site. Note the different depth and GVF scales.

of the wide range of uncertainties present in the gas transport equation. The model is orders of magnitude less sensible to the β and c_λ parameters (not shown).

[34] Simulated dissolution rates of 10–40 mM yr^{-1} (data not shown) are considerably lower than those obtained using the nonlocal transport term values by *Haeckel et al.* [2004] for methane hydrate dynamics (65–110 mM yr^{-1}). This difference can nevertheless be explained by the higher overall methane reaction rates in hydrate bearing sediments as compared to settings where gas is of biogenic origin [*Dale et al.*, 2008b; *Regnier et al.*, 2011].

4.4. Free Gas Phase and Microbial Reaction Dynamics

[35] Modeled yearly variations of the FGD (Figure 5) and the gas volume fraction (Figure 6) lag the temperature variations at the SWI at all sites due to the time required for heat to propagate into the sediment. Table 5 shows the monthly and depth-averaged gas volume fractions at the two sites. The highest monthly depth-averaged values were found in the early fall months at the pockmark and NRL sites due to the shallow FGD during this period. The amplitude for these monthly average variations also decreases with increasing FGD. For the NRL site, the depth-averaged gas volume fraction for June and July (0.00091) is comparable to the average according to bubble counts at the P6 site (0.0011) from *Anderson et al.* [1998]. In contrast, at a pockmark site, *Anderson et al.* [1998] found depth-averaged gas volume

fraction values for June and July which easily exceeded 0.01, which represents an order of magnitude higher than the values found at the modeled pockmark site. This discrepancy can be greatly attributed to the increasing-with-depth gas volume fractions measured by *Anderson et al.* [1998], which reach values of 0.09 at ~85 cm depth. A gas volume fraction of 0.09 represents 13.5 mM of methane gas at the local temperature and pressure, which is equivalent to twice the value of methane saturation concentration at the same conditions. Considering that the highest simulated methanogenesis rates at the pockmark site are in the order of 1.7 mM yr^{-1}

Table 5. Monthly and Depth-Averaged Gas Volume Fractions[a]

Month	Pockmark	NRL
January	1.2×10^{-3}	1.7×10^{-3}
February	3.3×10^{-4}	1.0×10^{-3}
March	8.4×10^{-5}	5.5×10^{-4}
April	2.3×10^{-4}	2.5×10^{-4}
May	9.1×10^{-4}	2.1×10^{-4}
June	2.0×10^{-3}	5.8×10^{-4}
July	2.8×10^{-3}	1.2×10^{-3}
August	3.3×10^{-3}	1.8×10^{-3}
September	3.4×10^{-3}	2.3×10^{-3}
October	3.3×10^{-3}	2.5×10^{-3}
November	2.8×10^{-3}	2.4×10^{-3}
December	2.1×10^{-3}	2.2×10^{-3}

[a]Depth averaging was performed over the gassy interval.
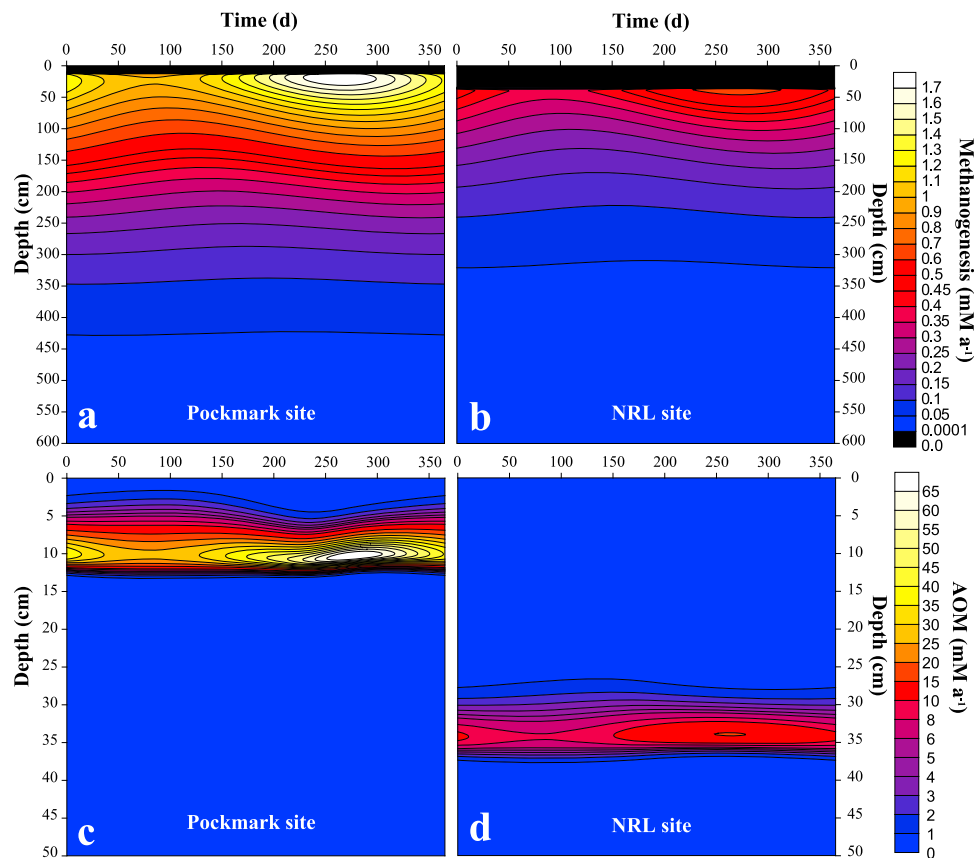
Figure 7. (a, b) Methanogenesis and (c, d) AOM rate profiles throughout the course of 1 year at the pockmark (Figures 7a and 7c) and NRL (Figures 7b and 7d) sites. The upper black top zone indicates the depth where sulfate reduction takes place. Note the nonlinear scale intervals.

(Figure 7), it seems highly unlikely that the deepest gas measured by *Anderson et al.* [1998] is due to the seasonal production and migration of free methane gas. Rather, the increasing gas volume fraction with depth at the pockmark site of *Anderson et al.* [1998] as opposed to our decreasing with depth trend (Figure 6) may be an indication that the deeper gas layers are the product of gas burial and accumulation over a long period of time. Although gas burial is not considered in these simulations, its impact on AOM and methane dynamics in general is likely to be minor over the temperature and pressure ranges in this study.

[36] Peaks in the gas volume fractions are of similar magnitude at both sites (~0.004). The position and thickness of the free gas layer nevertheless reveal large differences between sites with a yearly average FGD of ~25 and 65 cm at the pockmark and NRL sites respectively, and maximum thickness of ~85 cm at the pockmark and ~2 m at the NRL site. In addition, the FGD and the thickness of the gas layer are subjected to different seasonal fluctuations which are discussed in further detail below.

[37] The methanogenesis rate (Figure 7), the departure from saturation, and the free gas production/dissolution rates (Figure 8) vary over time with sediment depth due to the seasonality in heat propagation (Figures 1 and 2). At the pockmark site, high upward aqueous phase velocities compress the geochemical zonation toward the SWI as compared to the NRL site. Sulfate penetration is thus limited to the first decimeter at the pockmark site and AOM occurs

just below the SWI. At the NRL site, the SMTZ is located deeper (~35 cm sediment depth) and AOM rates are significantly lower. In line with the findings of *Dale et al.* [2008a] in Aarhus Bay, the seasonal shift of the SMTZ depth is low (~3 cm at pockmark and <1 cm at NRL). The methanogenesis zone begins at 15 cm depth at the pockmark as opposed to the 37 cm depth at the NRL site. In addition, high F_{POC} and v_a contribute toward higher maxima in the methanogenesis rates at the pockmark site as compared to the NRL site (Figure 7). Even with the increased methane production, however, the intruding freshwater from below maintains methane undersaturation in the deeper layers of the pockmark site, confining the zone of free gas production to the top 110 cm of the sediment, versus the ~300 cm limit at the NRL site (Figure 8). Therefore, although the levels of supersaturation and volumetric rates of methane gas production are slightly higher at the pockmark site than at NRL, the thinner zone where free gas can accumulate as it ascends toward the SWI explains why the free gas inventories remain lower at the pockmark site (Figure 6).

[38] Depth-integrated free gas production and dissolution rates display a large seasonal variability and occasionally greatly exceed the depth-integrated methanogenesis and AOM rates (Figure 9). In this case, they become the major sink/source terms for dissolved methane. Depth-integrated methanogenesis rates at the pockmark site are about twice those at the NRL site, but due to methane dilution by freshwater advection, the depth-integrated free gas forma-
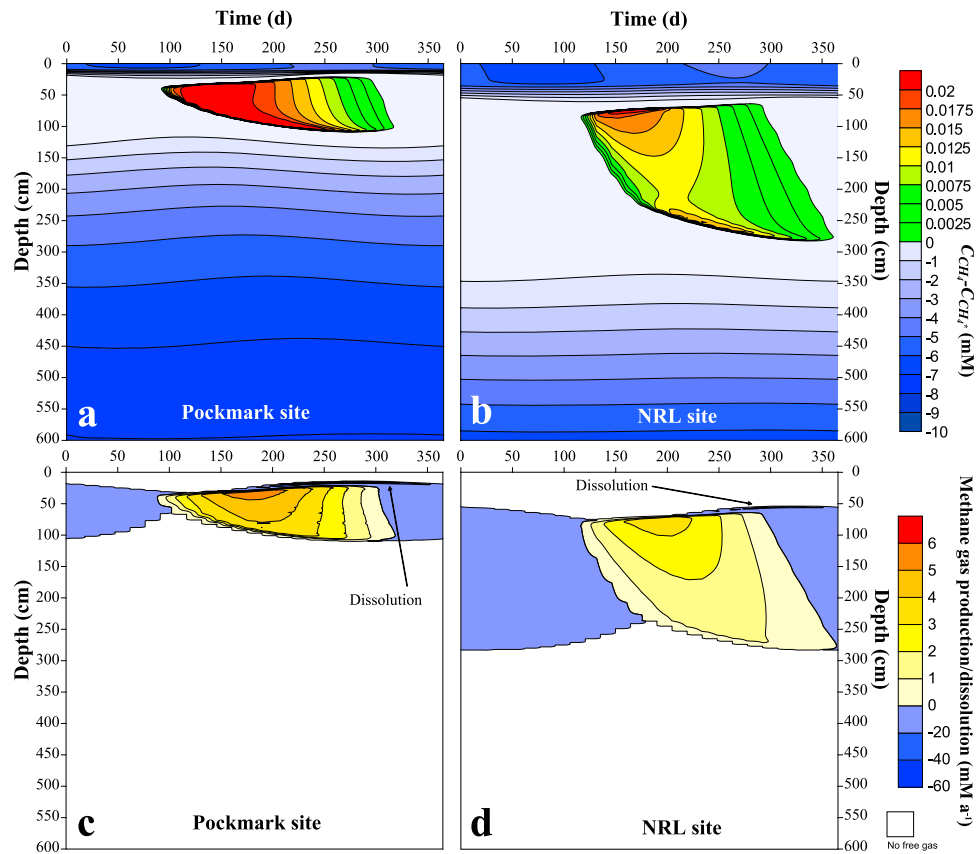
Figure 8. Departure from methane saturation ($C_{CH_4} - C_{CH_4}^*$) at (a) the pockmark and (b) NRL sites. Blue areas (negative values) indicate methane undersaturation where dissolution can potentially take place. Green-yellow-red areas (positive values) indicate areas of potential methane gas production. Methane gas production and dissolution at (c) the pockmark and (d) NRL sites. Blue areas indicate active dissolution whereas the green-yellow-red areas indicate methane gas production. Blank areas indicate absence of free methane gas. Note the nonlinear scale intervals for the positive regions and the negative regions.
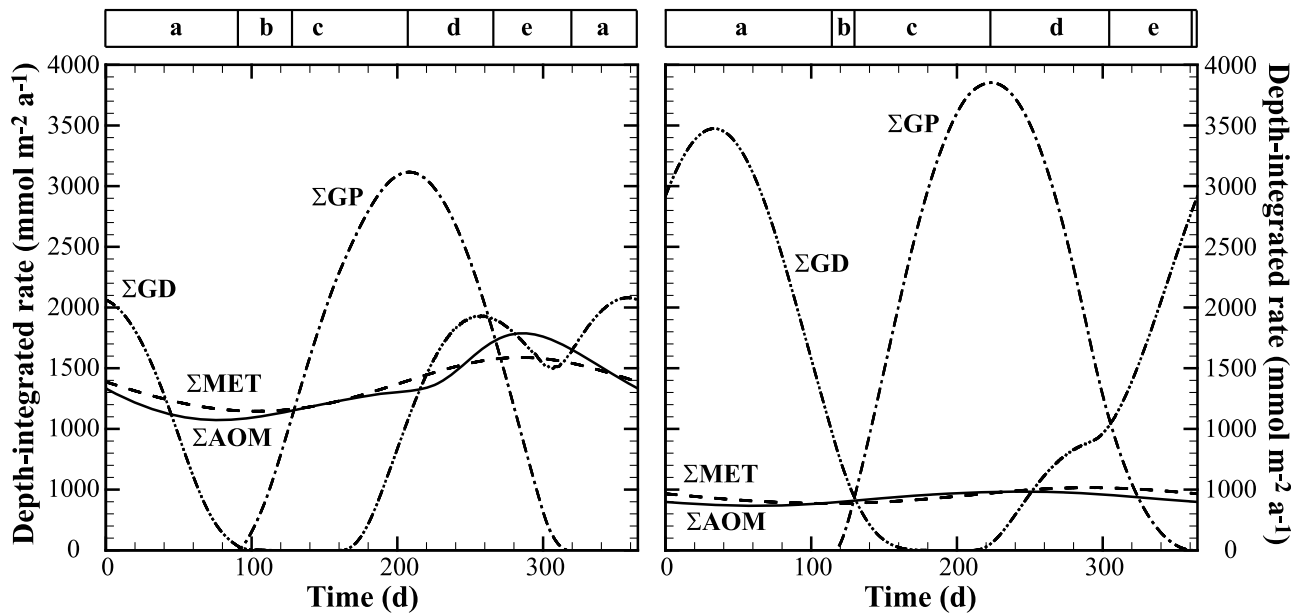
Figure 9. Seasonal trends for the depth-integrated rates of anaerobic oxidation of methane ($\sum$AOM), methanogenesis ($\sum$MET), methane gas production ($\sum$GP), and methane gas dissolution ($\sum$GD) at (left) the pockmark and (right) NRL sites. Time intervals a–e are discussed in the text.
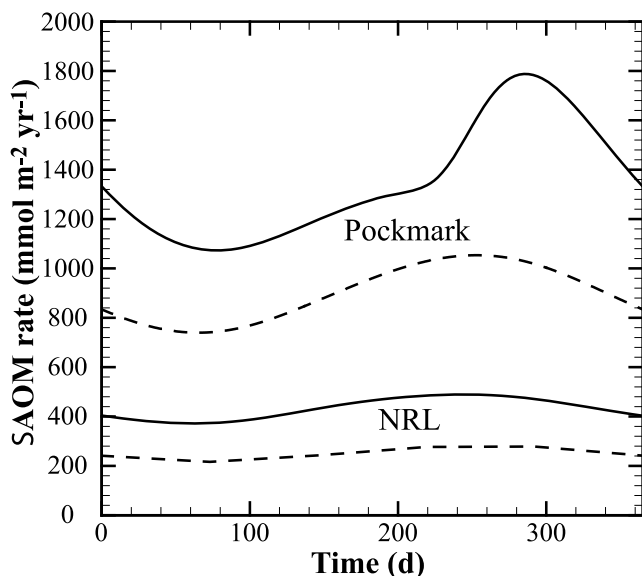
Figure 10. Yearly variation in depth-integrated AOM rates for the baseline simulations (solid lines) and those assuming no gas dissolution (dashed lines) at the pockmark and NRL sites.

tion values are actually smaller at the pockmark. Although the intensity of methanogenesis directly correlates with the in situ temperature in the sediment (Figure 7), free gas formation is stimulated by (1) the temperature increase, (2) the amount of supersaturated dissolved methane present in the free gas layer, and (3) the surface area of the available gas, with the more gas present the faster the reaction rate (equations (9) and (18)). This leads to a complex seasonal evolution of the geochemical rates affecting the gas phase as represented in Figure 9. During period a, the methanogenic zone is undersaturated, and the previously produced free methane gas is dissolving. During period b, the temperature-induced decrease in $C^*_{CH_4}$ and the increase in methanogenesis lead to oversaturation and free gas production. The integrated rate of free gas production exceeds the integrated methanogenesis rates in period c, and the dissolved methane inventories begin to decrease. The pace at which this inventory decreases, however, is too slow to keep up with the decreasing saturation concentrations triggered by rising temperatures, and the integrated rate of free gas production continues to increase. During period d the integrated rate of gas formation begins to decrease since the decrease in the dissolved methane inventory has overtaken the rate of decrease of the methane saturation concentrations. This deepens the undersaturated zone and increases the free gas migration and dissolution. Finally, during period e, depth-integrated free gas dissolution rates are greater than the depth-integrated free gas production rates and the gas inventory begins to decline, eventually leading to conditions that prevailed during period a.

[39] Although pore water advection is present at both the pockmark and the NRL site, the methane supply toward the SMTZ is governed by diffusion due to the large gradient forming in the upper reaches of the methanogenic zone (Figures 8c and 8d, narrow dark blue zone). The methane gradient, in turn, depends on the amount of gas dissolving. In

order to quantify the relative importance of each process on the seasonal variability in AOM rates, a model which assumes that all the gas produced escapes immediately the sediment (no gas dissolution) is compared with the results of simulations which allow for gas dissolution as it migrates toward the SWI (baseline model) (Figure 10). For the NRL site, the depth-integrated AOM rate for both models follows the same trend. This can be explained by the significantly shallower SMTZ depth (~30 cm depth in the sediment, Figure 7d) compared to the FGD (~65 cm, Figure 8d) at the NRL site. In this case, the migrating gas dissolves well below the SMTZ, and the dissolved methane which fuels AOM is transported almost entirely by diffusion. This indicates also that the seasonality in AOM can mostly be explained by the direct dependence of the rate on temperature and, to a lesser extent, to the temperature dependence on the diffusion coefficient (equations (7) and (8)). Redissolved gas accounts for about 40% of AOM when the FGD is deepest (around day 65) and about 55% when the FGD is shallowest (around day 245) at the NRL site. In contrast, the gas-explicit model at the pockmark site leads to dynamics that differ significantly from those of the model which ignores the feedback of the gas phase on AOM. The relative contribution of the free methane gas flux toward AOM is also more important than at the NRL site and sustains as much as 750 mmol m^{-2} yr^{-1} in late autumn (45%). At the pockmark, the SMTZ and FGD are closely located (<5 cm apart in the late autumn, Figures 7 and 8c and dissolution of gas co-occurs in the same sediment depths as AOM and thus leads to the second peak in depth-integrated AOM rates when the FGD is shallowest (around day 290).

4.5. FGD as an Indicator of AOM

[40] In gassy sediments where methane dissolution largely limits gas escape through ebullition, mass balance dictates that depth-integrated AOM can be equated to the sum of methane diffusive and gas fluxes ($F_{diff} + F_{gas}$), provided that fluid advection can be considered negligible. In this case, almost all the methane will be oxidized anaerobically, such that the depth integrated rate of AOM, $\sum AOM$, will equal $F_{diff} + F_{gas}$. Furthermore, on the basis of a steady state, pseudodiffusive model for the gas phase, *Dale et al.* [2009] described a strong nonlinear correlation between FGD, $C^*_{CH_4}$ and $\sum AOM$ in the shallow sediments of Aarhus Bay where upward fluid flow was absent. A series of predictive equations was proposed, allowing for the calculation of the total methane flux, and thus $\sum AOM$, from the FGD and the $C^*_{CH_4}$. These relationships, established for a range of FGD between 600 and 100 cm, are particularly appealing as they provide a means to quantify $\sum AOM$ from two parameters (FGD, $C^*_{CH_4}$) that are readily determinable over large areas of the seafloor through noninvasive techniques. Figure 11 shows the power law relationships between FGD and methane flux toward the SMTZ (assumed to be equivalent to $\sum AOM$) derived by *Dale et al.* [2009], extended here to shallower free gas depths (20 cm). Superimposed on these predictive curves are the seasonal evolution of FGD versus $\sum AOM$ for the two locations in Eckernförde Bay with active fluid flow. The seasonality of $C^*_{CH_4}$ in the SMTZ for the two sites varies from about 5.5 mM to about 8 mM (Figure 3) and thus fall within the end-member values investigated by *Dale et al.* [2009]. Although the general trend established on the basis of the
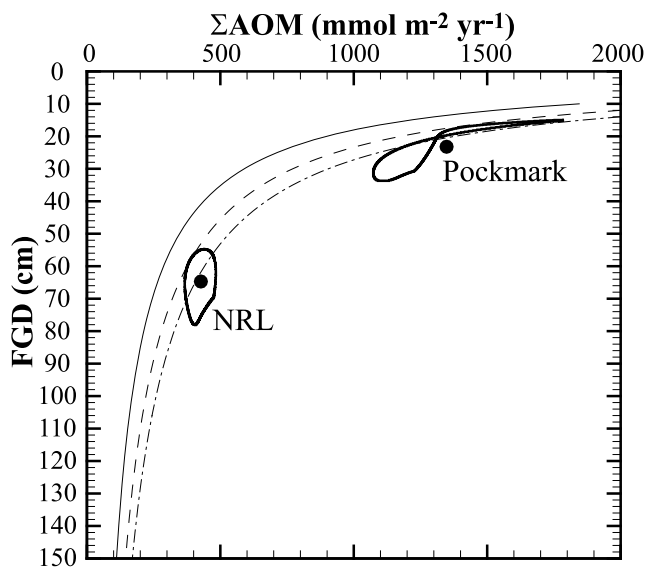
Figure 11. Free gas depth (FGD) versus depth-integrated AOM rates ($\sum AOM$) for the NRL and pockmark. The thin black lines represent power law functions derived by *Dale et al.* [2009] for 5 mM (solid line), 7 mM (dashed line) and 9 mM (dash dotted line) methane solubility concentrations. The points represent the yearly simulated average, whereas the thick lines represent the simulated seasonal trends for each site.

present results at both sites provides slightly deeper FGDs for the corresponding $\sum AOM$ as compared to *Dale et al.* [2009], the values fall within error estimates of *Dale et al.* [2009] and they conform to the same power law dependency. It can thus be inferred that the algorithm of *Dale et al.* [2009] can be extrapolated to much shallower FGDs, even in sediments with moderately high rates of fluid advection. Yet, although the sites with the shallowest FGD exhibit the highest depth-integrated AOM rates, the seasonal variations in FGD and $\sum AOM$ exhibit a hysteresis-type behavior, that is, two values of $\sum AOM$ can be obtained for the same FGD. This arises as a result of the seasonal displacement of the gas layer and the SMTZ in addition to the temperature response on the kinetic rate law for the biologically mediated reactions. This further causes the model-predicted $\sum AOM$ to extend further beyond the curves predicted by *Dale et al.* [2009] which are due to variations in solubility only. At the pockmark site when the FGD is shallowest, the proximity of the gas dissolution zone to the SMTZ (Figure 10) results in a proportional variation between $\sum AOM$ and FGD and the looping is attenuated. Nevertheless, it is clear that these seasonally resolved results, resting on a fully resolved model for the gas phase, provide additional support for the predictive relationship by *Dale et al.* [2009] and extend its range of applicability in marine sediments.

5. Model Limitations

[41] In our model, three-phase flow equations are applied to sediments where the solid, aqueous, and gaseous phases migrate at different rates, with the fluid phases moving in opposite direction to the solid phase. In our model, the gas bubbles are treated as a continuum fluid moving through

(and with) another fluid phase under the effect of buoyancy and other external pressure gradients, according to the Darcy law. The permeability takes implicitly into account the resistance of the porous medium to the motion of the gas phase. What we call "radius" is only an effective measure of gas volume fraction (through equation (A13)).

[42] This mechanism is difficult to validate, since interstitial gas movement within the sediment has not been directly measured. Nevertheless, as discussed previously, field observations of steep methane gradients and unusually high AOM rates have been used as indirect evidence for the dissolution of methane bubbles in the undersaturated zone of Eckernförde Bay sediments. Within the assumptions of our model approach, we propose a viable, yet speculative mechanism which is in accord with such observations. Using different assumptions, gas bubbles could either fracture the sediment and quickly migrate to the overlying water, become buried or entrained by the upward aqueous without instigating additional gas movement.

[43] A two-dimensional model which incorporates both the ability for gas to migrate through the pore space and the ability to fracture the sediment was discussed by *Jain and Juanes* [2009]. The authors established a theoretical framework to compare upward gas migration through capillary invasion versus fracture formation and found that grain size is a determinant factor. In their model, a grain size diameter of 0.1 μm is the threshold value below which fracture formation becomes dominant. In sediments with larger grain sizes it is thus possible to have capillary invasion provided that the excess gas pressure overcome the entry pressure of the pore throats. Considering that gas fracture was not witnessed at our sites, and that most of the sediment grains sizes in Eckernförde Bay are of silt size (>2 μm), we consider the case of whether the entry pressure can be exceeded in Eckernförde Bay sediments. Here, entry pressures fall in the 10 kPa range [*Jain and Juanes*, 2009]. If we assume that the excess gas pressure in a spherical bubble is given by $2\sigma/r$ [*Rosner and Epstein*, 1972], with σ as the surface tension ($\sigma = 50 \times 10^{-3}$ N/m) then the bubble radii which are required to exceed the entry pressure would be less than 10 μm. While these bubbles are considerably smaller than the maximum average bubble radii from the simulations, it is conceivable that our mechanism takes place during the early stages of seasonal bubble formation when these are small in size. However, even in the case of larger bubbles, our mechanism is still possible, since movement of water through these pores may lead to a reduction in the entry pressure by deforming the bubble shape, thus changing the contact angle between the gas and the water phases.

[44] Furthermore, it is likely that the large heterogeneities present in the sediment properties may lead to bubble growth rates and movement which are diverse, that is, every bubble behaves differently. For instance, both interstitial upward bubble movement through our proposed mechanism and gas burial could occur concomitantly within the sediment depending on the pore space, the shape of the bubbles and the pressure exerted by the upward moving fluid around each individual bubble. Our approach should thus be considered as one possible end-member of bubble movement in unfractured sediments. It could be expanded to include both gas burial and interstitial bubble movement, with factors such as higher compaction, increasing grain sizes and larger

pore throats acting probably in favor of the active upward gas movement at the expense of gas burial.

6. Conclusions

[45] The seasonal dissolved and gaseous methane profiles and associated reaction rates in Eckernförde Bay (Germany) are strictly controlled by temperature variations, with only marginal contributions from the sea level variations due to tides. The dissolved methane concentration is governed by the activity of microbially mediated reactions which are a source (methanogenesis) or sink (AOM) for dissolved methane, in addition to the effects of methane gas formation and dissolution, all of which are temperature sensitive. At the NRL site, the seasonal trends in methane turnover rates and free gas depth (FGD) do not coincide due to the distance between the SMTZ (where AOM takes place) and the zone of gas formation, and time lags in heat and gas transport. At a pockmark site, however, free gas dissolution close to the SMTZ in autumn provides a direct methane source for AOM, and the depth-integrated AOM rates essentially parallel the trend in the FGD.

[46] At both of the investigated sites, the interstitial gas velocity calculated by our speculative mechanism is too small to allow the gas to migrate past the AOM zone and escape the sediment. Ultimately, by driving pore water undersaturation and gas dissolution, AOM is an effective barrier for advecting methane gas in unfractured sediments. Ebullition is thus most likely to occur in settings where gas volume fractions are higher than those simulated in this study (>1.0%), such as Cape Lookout Bight where volumes of >10 % are typical [e.g., *Martens and Klump*, 1980] and the radius size of the bubble is large enough for bubbles to fracture the sediment [*Algar et al.*, 2011]. At the present study sites, the application of FGD as an indicator of depth-integrated AOM rates and the methane flux to the SMTZ has also been corroborated by the present fully resolved model for the gas phase. This extended relationship is particularly appealing as it provides a means to estimate regional methane turnover rates in gassy sediments through noninvasive acoustic techniques.

Appendix A: Equation Derivation

[47] The 1-D reaction-transport model accounts for mass and volume conservation for the solid, aqueous, and gaseous phase and chemical species residing within these phases. The model development follows that of *Mogollón et al.* [2009] but includes the compressibility factor of an ideal gas phase. Mass conservation for the three phases states that:

$$\frac{\partial \phi_s \rho_s}{\partial t} = -\frac{\partial \phi_s \rho_s v_s}{\partial z} + \rho_s \Sigma R_s \tag{A1}$$

$$\frac{\partial \phi_a \rho_a}{\partial t} = -\frac{\partial \phi_a \rho_a v_a}{\partial z} - \frac{\Re T}{P} \rho_a \varphi R_{GAS} - \rho_a \Sigma R_s \tag{A2}$$

$$\frac{\partial \phi_g \rho_g}{\partial t} = -\frac{\partial \phi_g \rho_g v_g}{\partial z} + \frac{\Re T}{P} \varphi \rho_g R_{GAS} \tag{A3}$$

where t is time, z is the vertical coordinate defined as positive downward from the sediment-water interface (SWI),

and ρ, ϕ, v represent the phase-specific density, volume fraction, and velocity due to sediment burial, respectively. $\Re$ is the universal gas constant, T is temperature, P is pressure. R_{GAS} is defined in equation (18), ΣR_s describes the net molar transfer rate between all solid phases and the aqueous phase, and φ represents the porosity.

[48] Volume conservation is dictated through (equation (A4)), whereas the porosity is defined in equation (A5):

$$\phi_a + \phi_g + \phi_s = 1 \tag{A4}$$

$$\varphi = \phi_a + \phi_g \tag{A5}$$

[49] Assuming steady state compaction ($\partial \varphi / \partial t = 0$), an exponential relation between porosity and effective stress of the sediment, σ, through a "sediment compressibility coefficient, b" [$\varphi = \varphi_\infty + (\varphi_\infty - \varphi_0)e^{(-\sigma b)}$] [*Boudreau and Bennett*, 1999], and sinusoidal temporal variations in the temperature and pressure (equations (23) and (24), respectively), these equations can be combined, and integrated over depth to obtain the final equation describing sediment compaction (for step by step derivation, see *Mogollón et al.* [2009]):

$$\frac{\partial \varphi}{\partial z} = \frac{-b(\varphi - \varphi_\infty)(1 - \varphi)^2}{\varepsilon d^2 \left(\phi_a^3/\eta_a + \phi_g^3/\eta_g\right)} \left(A - \frac{v_s|_0 (1 - \varphi_0)}{(1 - \varphi)} - \varepsilon d^2 \frac{B - D}{(1 - \varphi)^2} \right.$$
$$\left. - (1 - \varphi)^{-1} \int_0^z \Sigma R_s dz - \int_0^z Q dz \right) \tag{A6}$$

where Q is a function representing the pressure and temperature effects on gas compressibility:

$$Q = \phi_g \left(\frac{v_g}{P} \frac{\partial P}{\partial z} - \frac{v_g}{T} \frac{\partial T}{\partial z} \right) + \phi_g \left(\frac{2A_{sea}\rho_a g \pi}{P\tau} \cos\left(2\pi \frac{(t + \theta_{sea})}{\tau}\right) \right.$$
$$\left. - \frac{2A_0 \pi}{T\tau} \cos\left(2\pi \frac{(t + \theta_0)}{\tau}\right) \right) \tag{A7}$$

A is the integration constant:

$$A = \frac{(1 - \varphi_0)}{(1 - \varphi_L)} v_s|_0 + \frac{\int_0^L \Sigma R_s dz}{(1 - \varphi_L)} + q_a|_L + q_g|_L + \int_0^L Q dz \tag{A8}$$

where $v_s|_0$ is the burial velocity of solids at the SWI, and $q_a|_L$ and $q_g|_L$ are the aqueous and gaseous flows at the lower boundary respectively

$$q_a|_L = (\phi_a|_L v_a|_L - \phi_a|_L v_s|_L) \tag{A9}$$

$$q_g|_L = (\phi_g|_L v_g|_L - \phi_g|_L v_s|_L) \tag{A10}$$

Equation (A7) was derived assuming that, in terms of compressibility, the gas pressure was the same as the pore water pressure. In other words, bubble surface tension effects were ignored since they only have an effect on very small bubbles.

[50] In the derivation of equation (A6), and throughout the model, the following equations were used to determine the burial velocity of solids and the aqueous phase velocity:

$$v_s = \frac{(1 - \varphi_0)v_s|_0}{(1 - \varphi)} + \frac{\int_0^z \Sigma R_s dz}{(1 - \varphi)} \qquad (A11)$$

$$v_a = \frac{q_a|_L + q_g|_L + v_s|_L - (1 - \varphi)v_s - \phi_g v_g + \int_z^L Q dz}{\phi_a} \qquad (A12)$$

Equation (9) derives from equation (A3) by relating the gas volume fraction (ϕ_g) to the average bubble radius (r) of the collective gas phase:

$$\phi_g = \frac{4}{3}\pi r^3 n \varphi \qquad (A13)$$

where n is the number of bubbles per pore volume, or bubble density. n is assumed to be constant in time and depth in the model. The gas phase density, ρ_g, for an ideal gas is defined as:

$$\rho_g = \frac{MP}{\Re T} \qquad (A14)$$

where M is the methane molecular weight. Substituting equations (18), (A13), and (A14), and canceling out the constant terms M, n, $\Re$, and 4π, yields the following relation:

$$\frac{\partial \varphi r^3 P/T}{\partial t} = -\frac{\partial \varphi v_g r^3 P/T}{\partial z} + 3r^2 \varphi \frac{P}{T}\psi \qquad (A15)$$

With the assumption of steady state compaction ($\partial \varphi/\partial t = 0$) the φ term can be pulled out of the left hand side of the equation, yielding

$$\frac{\partial r^3 P/T}{\partial t} = -\varphi^{-1}\frac{\partial \varphi v_g r^3 P/T}{\partial z} + 3r^2 \frac{P}{T}\psi \qquad (A16)$$

[51] The continuity equation for the number of bubbles assuming negligible bubble nucleation ($\partial \varphi n/\partial t = \partial \varphi n v_g/\partial z$) can further be used to simplify equation (A16). If n is assumed constant and steady state compaction is assumed, then $\partial \varphi v_g/\partial z = 0$, and equation (A16) can be simplified to equation (9).

Appendix B: Bubble Growth Calibration

[52] Bubble growth rates were calibrated by scaling the time-dependent radius growth function (equation (B1)) with that of the diffusion-limited constant eccentricity (DLCE) model [*Gardiner et al.*, 2003b]. DLCE bubble growth rates, in turn, are in quantitative agreement with the linear elastic fracture mechanics (LEFM) growth rates [*Gardiner et al.*, 2003a].

[53] Integrating equation (9) for a nonmigrating bubble [$\partial(v_g \phi_g P/T)/\partial z = 0$] yields a bubble growth equation (equation (B1)) which can be compared with previously developed algorithms for bubble growth. For instance, the growth of a bubble in the DLCE model [*Gardiner et al.*,

2003b], adapted to our nomenclature is portrayed for comparison purposes (equation (B2)).

$$r = \sqrt{D\frac{2\Re T\left(C_{CH_4} - C^*_{CH_4}\right)}{Pc_\lambda}t + r_0^2} \qquad (B1)$$

$$r = \sqrt{\frac{2D\Re T}{P}\frac{\sqrt{1 - E_{cc}^2}}{E_{cc}^{1/3}}\frac{SR_1^2/(6D) + \left(C_{CH_4} - C^*_{CH_4}\right)}{\arccos(E_{cc})}t + r_0^2} \qquad (B2)$$

where r_{eq} is the equivalent bubble radius, t is time, D is the diffusion coefficient, $\Re$ is the universal gas constant, T is the temperature, P is the pressure, R_1 is the outer boundary of the 'radial' model, centered around a gas bubble, ($C_{CH_4} - C^*_{CH_4}$) is the departure from saturation at R_1, S is the rate of methanogenesis within the model domain, r_0 is the initial radius and E_{cc} is the bubble aspect ratio.

[54] Typical values for S, R_l and ($C_{CH_4} - C^*_{CH_4}$) in Eckernförde Bay are 0.1 mM yr^{-1}, 1 cm and 0.1–1 mM, respectively. Thus, the in situ production term $SR_1^2/(6D)$ is negligible in comparison to the supersaturation term ($C_{CH_4} - C^*_{CH_4}$). Under these conditions, the two models give identical results if:

$$c_\lambda = \frac{\arccos(E_{cc})E_{cc}^{1/3}}{\left(1 - E_{cc}^2\right)^{0.5}} \qquad (B3)$$

Using the value of E_{cc}, which in the work by *Gardiner et al.* [2003a] best represented LEFM growth times for a 500 mL bubble, gives a value of c_λ equal to 0.51. *Algar and Boudreau* [2009], however, corrected the LEFM algorithm and found growth times for a 500 mL bubble that were 27% lower than those proposed by *Gardiner et al.* [2003a]. This correction can be translated into our growth algorithm by adjusting the value for c_λ to 0.38.

References

Abegg, F., and A. L. Anderson (1997), The acoustic turbid layer in muddy sediments of Eckernförde Bay, Western Baltic: methane concentration, saturation and bubble characteristics, *Mar. Geol.*, *137*, 137–147, doi:10.1016/S0025-3227(96)00084-9.

Albert, D. B., C. S. Martens, and M. J. Alperin (1998), Biogeochemical processes controlling methane in gassy coastal sediments-Part 2: groundwater flow control of acoustic turbidity in Eckernförde Bay sediments, *Cont. Shelf Res.*, *18*, 1771–1793, doi:10.1016/S0278-4343(98)00057-0.

Algar, C., and B. Boudreau (2009), Transient growth of an isolated bubble in muddy, fine-grained sediments, *Geochim. Cosmochim. Acta*, *73*(9), 2581–2591, doi:10.1016/j.gca.2009.02.008.

Algar, C. K., B. P. Boudreau, and M. A. Barry (2011), Initial rise of bubbles in cohesive sediments by a process of viscoelastic fracture, *J. Geophys. Res.*, *116*, B04207, doi:10.1029/2010JB008133.

Anderson, A. L., F. Abegg, J. A. Hawkins, M. E. Duncan, and A. P. Lyons (1998), Bubble populations and acoustic interaction with the gassy floor of Eckernförde Bay, *Cont. Shelf Res.*, *18*, 1807–1838, doi:10.1016/S0278-4343(98)00059-4.

Boudreau, B. (1997), *Diagenetic Models and Their Implementations*, Springer-Verlag, Berlin.

Boudreau, B. P., and R. H. Bennett (1999), New rheological and porosity equations for steady-state compaction, *Am. J. Sci.*, *299*(7-9), 517–528, doi:10.2475/ajs.299.7-9.517.

Boudreau, B. P., C. Algar, B. D. Johnson, I. Croudace, A. Reed, Y. Furukawa, K. M. Dorgan, P. A. Jumars, A. S. Grader, and B. S. Gardiner (2005), Bubble growth and rise in soft sediments, *Geology*, *33*(6), 517–520.

Buffett, B., and D. Archer (2004), Global inventory of methane clathrate: sensitivity to changes in the deep ocean, *Earth Planet. Sci. Lett.*, *227*(3–4), 185–199, doi:10.1016/j.epsl.2004.09.005.

Bussmann, I., P. R. Dando, S. J. Niven, and E. Suess (1999), Groundwater seepage in the marine environment: role for mass flux and bacterial activity, *Mar. Ecol. Progr. Ser.*, *178*, 169–177.

Claypool, G., and I. Kaplan (1974), The origin and distribution of methane in marine sediments, in *Natural Gases in Marine Sediments*, edited by I. Kaplan, pp. 99–139, Plenum, New York.

Crill, P. M., and C. S. Martens (1983), Spatial and temporal fluctuations of methane production in anoxic coastal marine sediments, *Limnol. Oceanogr.*, *86*, 1117–1130.

Dale, A. W., D. R. Aguilera, P. Regnier, H. Fossing, N. J. Knab, and B. B. Jørgensen (2008a), Seasonal dynamics of the depth and rate of anaerobic oxidation of methane in Aarhus Bay (Denmark) sediments, *J. Mar. Res.*, *66*, 127–155.

Dale, A. W., P. Van Cappellen, D. R. Aguilera, and P. Regnier (2008b), Methane efflux from marine sediments in passive and active margins: Estimations from bioenergetic reaction-transport simulations, *Earth Planet. Sci. Lett.*, *265*, 329–344, doi:10.1016/j.epsl.2007.09.026.

Dale, A. W., P. Regnier, P. Van Cappellen, H. Fossing, J. B. Jensen, and B. B. Jørgensen (2009), Remote quantification of methane fluxes in gassy marine sediments through seismic survey, *Geology*, *37*(3), 235–238, doi:10.1130/G25323A.1.

Davie, M. K., and B. A. Buffett (2001), A numerical model for the formation of gas hydrate below the seafloor, *J. Geophys. Res.*, *106*(B1), 497–514.

Duan, Z., and S. Mao (2006), A thermodynamic model for calculating methane solubility, density and gas phase composition of methane-bearing aqueous fluids from 273 to 523 k and from 1 to 2000 bar, *Geochim. Cosmochim. Acta*, *70*(13), 3369–3386, doi:10.1016/j.gca.2006.03.018.

Ehrhardt, M., K. Grasshoff, K. Kremling, and T. Almgren (1983), *Methods of Seawater Analysis*, 2nd rev., 419 pp., Verlag Chemie, Weinheim, Germany.

Gardiner, B. S., B. P. Boudreau, and B. D. Johnson (2003a), Growth of disk-shaped bubbles in sediments, *Geochim. Cosmochim. Acta*, *67*(8), 1485–1494.

Gardiner, B. S., B. P. Boudreau, and B. D. Johnson (2003b), Slow growth of an isolated disk-shaped bubble of constant eccentricity in the presence of a distributed gas source, *Appl. Math. Modell.*, *27*(10), 817–829, doi:10.1016/S0307-904X(03)00086-6.

Haeckel, M., E. Suess, K. Wallmann, and D. Rickert (2004), Rising methane gas bubbles form massive hydrate layers at the seafloor, *Geochim. Cosmochim. Acta*, *68*(21), 4335–4345, doi:10.1016/j.gca.2004.01.018.

Haeckel, M., B. P. Boudreau, and K. Wallmann (2007), Bubble-induced porewater mixing: A 3-d model for deep porewater irrigation, *Geochim. Cosmochim. Acta*, *71*, 5135–5154.

Jain, A. K., and R. Juanes (2009), Preferential mode of gas invasion in sediments: Grain-scale mechanistic model of coupled multiphase fluid flow and sediment mechanics, *J. Geophys. Res.*, *114*, B08101, doi:10.1029/2008JB006002.

Jensen, J. B., A. Kuijpers, O. Bennike, T. Laier, and F. Werner (2002), New geological aspects for freshwater seepage and formation in Eckernförde Bay, western Baltic, *Cont. Shelf Res.*, *22*(15), 2159–2173, doi:10.1016/S0278-4343(02)00076-6.

Jørgensen, B. B. (1977), The sulfur cycle of a coastal marine sediment (Limfjorden, Denmark), *Limnol. Oceanogr.*, *22*, 814–832.

Jørgensen, B. B., and S. Kasten (2006), Sulfur cycling and methane oxidation, in *Marine Geochemistry*, pp. 271–309, 2nd ed., Springer, Berlin.

Laier, T., and J. B. Jensen (2007), Shallow gas depth-contour map of the Skagerrak-western Baltic Sea region, *Geo-Mar. Lett.*, *27*(2–4), 127–141.

Martens, C. S., and J. V. Klump (1980), Biogeochemical cycling in an organic-rich coastal marine basin-I. Methane sediment-water exchange processes, *Geochim. Cosmochim. Acta*, *44*(3), 471–490.

Martens, C. S., D. B. Albert, and M. J. Alperin (1998), Biogeochemical processes controlling methane in gassy coastal sediments - Part 1. A model coupling organic matter flux to gas production, oxidation and transport, *Cont. Shelf Res.*, *18*(14–15), 1741–1770, doi:10.1016/S0278-4343(98)00056-9.

Martens, C. S., D. B. Albert, and M. J. Alperin (1999), Stable isotope tracing of anaerobic methane oxidation in the gassy sediments of Eckernförde Bay, German Baltic Sea, *Am. J. Sci.*, *299*(7–9), 589–610, doi:10.2475/ajs.299.7-9.589.

Mogollón, J. M., I. L'Heureux, A. W. Dale, and P. Regnier (2009), Methane gas-phase dynamics in marine sediments: A model study, *Am. J. Sci.*, *309*, 189–220, doi:10.2475/03.2009.01.

Nittrouer, C. A., G. R. Lopez, L. D. Wright, S. J. Bentley, A. F. D'Andrea, C. T. Friedrichs, N. I. Craig, and C. K. Sommerfield (1998), Oceanographic processes and the preservation of sedimentary structure in Eckernförde Bay, Baltic Sea, *Cont. Shelf Res.*, *18*, 1686–1714, doi:10.1016/S0278-4343(98)00054-5.

Reeburgh, W. S. (2007), Oceanic methane biogeochemistry, *Chem. Rev.*, *107*(2), 486–513, doi:10.1021/cr050362v.

Regnier, P., A. Dale, S. Arndt, D. LaRowe, J. Mogollón, and P. V. Cappellen (2011), Quantitative analysis of anaerobic oxidation of methane (aom) in marine sediments: A modeling perspective, *Earth Sci. Rev.*, *106*(1–2), 105–130, doi:10.1016/j.earscirev.2011.01.002.

Rosner, D. E., and M. Epstein (1972), Effects of interface kinetics, capillarity and solute diffusion on bubble growth rates in highly supersaturated liquids, *Chem. Eng. Sci.*, *27*(1), 69–88, doi:10.1016/0009-2509(72)80142-8.

Schlüter, M., E. J. Sauter, H.-P. Hansen, and E. Suess (2000), Seasonal variations of bioirrigation in coastal sediments: Modelling of field data, *Geochim. Cosmochim. Acta*, *64*(5), 821–834.

Schlüter, M., E. J. Sauter, C. E. Andersen, H. Dahlgaard, and P. R. Dando (2004), Spatial distribution and budget for submarine groundwater discharge in Eckernförde Bay (Western Baltic Sea), *Limnol. Oceanogr.*, *49*(1), 157–167.

Silva, A. J., and H. G. Brandes (1998), Geotechnical properties and behavior of high-porosity, organic-rich sediments in Eckernförde Bay, Germany, *Cont. Shelf Res.*, *18*(14–15), 1917–1938, doi:10.1016/S0278-4343(98)00063-6.

Stöhr, M., and A. Khalili (2006), Dynamic regimes of buoyancy-affected two-phase flow in unconsolidated porous media, *Phys. Rev. E*, *73*(3), 03630.

Treude, T., M. Krüger, A. Boetius, and B. B. Jørgensen (2005), Environmental control on anaerobic oxidation of methane in the gassy sediments of Eckernförde Bay (German Baltic), *Limnol. Oceanogr.*, *50*(6), 1771–1786.

Wever, T. F., and H. M. Fiedler (1995), Variability of acoustic turbidity in Eckernförde Bay (southwest Baltic Sea) related to the annual temperature cycle, *Mar. Geol.*, *125*(1–2), 21–27.

Wever, T. F., F. Abegg, H. M. Fiedler, G. Fechner, and I. H. Stender (1998), Shallow gas in the muddy sediments of Eckernförde Bay, Germany, *Cont. Shelf Res.*, *18*(14–15), 1715–1740, doi:10.1016/S0278-4343(98)00055-7.

Wever, T. F., R. Lühder, H. Voß, and U. Knispel (2006), Potential environmental control of free shallow gas in the seafloor of Eckernförde Bay, Germany, *Mar. Geol.*, *225*, 1–4.

Whiticar, M. J. (2002), Diagenetic relationships of methanogenesis, nutrients, acoustic turbidity, pockmarks and freshwater seepages in Eckernförde Bay, *Mar. Geol.*, *182*(1–2), 29–53.

Woodside, W., and J. H. Messmer (1961), Thermal conductivity of porous media. I. Unconsolidated sands, *J. Appl. Phys.*, *32*(9), 1688–1699, doi:10.1063/1.1728419.

A. W. Dale, Leibniz-Institut für Meereswissenschaften, IFM-GEOMAR, Gebude Ostufer, Wischhofstr. 1-3, Geb. 8D, Room 109, D-24148 Kiel, Germany. (adale@ifm-geomar.de)

I. L'Heureux, Department of Physics, University of Ottawa, MacDonald Hall, 150 Louis Pasteur, Ottawa, ON K1N 6N5 Canada. (ilheureu@uottawa.ca)

J. M. Mogollón, Department of Earth Sciences, Utrecht University, PO Box 80.021, NL-3508 TA, Utrecht, Netherlands. (mogollon@geo.uu.nl)

P. Regnier, Département des Sciences de la Terre et de l'Environnement, Université Libre de Bruxelles, 50 Av. F.D. Roosevelt, B-1050 Brussels, Belgium. (pregnier@ulb.ac.be)